10-16-2023

# Homonuclear Ultracold Elastic *s*-wave Collisions of Alkali-Metal Atoms via Multichannel Quantum Defect Theory

Alyson T. Laskowski
*Trinity University*, alaskows@trinity.edu

Nirav P. Mehta
*Trinity University*, nmehta@trinity.edu

# Homonuclear ultracold elastic *s*-wave collisions of alkali-metal atoms via multichannel quantum defect theory

Alyson Laskowski [*] and Nirav P. Mehta [†]

*Department of Physics and Astronomy, Trinity University, San Antonio, Texas 78212, USA*

Multichannel quantum-defect theory (MQDT) provides a powerful toolkit for describing and understanding collisions of cold alkali-metal atoms. Various MQDT approximations differ primarily in how they characterize the so-called short-ranged *K* matrix $\mathbf{K}_{sr}$, which encapsulates the short-ranged physics into a handful of low-energy parameters that exhibit simple and smooth dependence on energy and field. Here, we compare three different methods for computing $\mathbf{K}_{sr}$ for homonuclear collisions of alkali-metal atoms, from lithium to cesium. The MQDT calculations are benchmarked against numerically converged coupled-channels calculations that use a log-derivative propagator out to the asymptotic region. We study how well these approximations reproduce positions of *s*-wave magnetic Feshbach resonances, comparing with experiment where possible, and identify the limitations of various approximations.

## I. INTRODUCTION

The ability to control the scattering length by tuning an applied magnetic field in the vicinity of a magnetic Feshbach resonance has now become a standard tool in experimental ultracold physics [1]. For example, manipulation of the scattering length in this manner plays a key role in the realization of strongly interacting many-body systems [2]. It enables the creation of loosely bound molecules via Feshbach association, which is the first step in the formation of deeply bound molecules by subsequent stimulated Raman adiabatic passage [3]. Control of the two-body scattering length in this manner has played a key role in the study of Efimov physics [4–9]. Theoretical developments have kept pace with experiment in predicting and understanding the properties of magnetic Feshbach resonances [1], and one of the most powerful theoretical tools that has been brought to bear upon the problem is multichannel quantum-defect theory (MQDT).

MQDT provides a powerful formalism for computing and understanding the field and energy dependence of collisional cross sections in ultracold systems. It has a long history, with seminal contributions made by many authors [10–21]. Various formulations differ significantly in notation and scope, but not in spirit. MQDT at its heart leverages a separation of energy and length scales in order to simplify the calculation of low-energy observables. It is in this sense an "effective theory" similar in spirit to modern renormalization techniques and effective-field theories. In its application to ultracold atomic collisions, it can be made to agree with coupled channels calculations to a numerical accuracy approaching exactness.

The strength and nature of ultracold collisions depends on the separation distance *R* between atoms. At small *R*,

the wells of the ground-state spin-singlet and spin-triplet Born-Oppenheimer potentials are many orders of magnitude deeper than any other relevant energy scale, including those of the long-range van der Waals tail and one-atom hyperfine-Zeeman interactions. This robust separation of energy and length scales enables one to treat the collision in stages. First, one solves the short-range problem to determine a short-range *K* matrix $\mathbf{K}_{sr}$, which is defined with respect to energy-analytic reference functions $\{\hat{f}, \hat{g}\}$ that are solutions to the long-range (e.g., van der Waals) potential common to all collision channels. Then one treats the long-range physics using the methods of MQDT, which involve accounting for (1) the phase accumulated in the long-range potential by $\{\hat{f}, \hat{g}\}$—both with respect to each other and with respect to a pair of energy-normalized solutions $\{f, g\}$, (2) the energy-normalization of $\{f, g\}$, particularly when expressed in terms of the energy-analytic pair $\{\hat{f}, \hat{g}\}$, and (3) the exponentially decaying asymptotic form of the wave function in closed channels.

The short-range *K* matrix is viewed as "input" into the machinery of MQDT, encoding information about the short-range physics relevant to low-energy (near threshold) observables. Moreover, $\mathbf{K}_{sr}$ exhibits a smooth and simple dependence on both energy and magnetic field. Therefore, it only needs to be calculated on a coarse grid of energy and field values to provide a complete description of the short-range physics. The frame transformation (FT) [22] provides a powerful tool for approximating $\mathbf{K}_{sr}$ by writing it in terms of the singlet and triplet quantum defects $\mu_S$ and a sum over the spin singlet ($S = 0$) and spin triplet ($S = 1$) projection operators. A recoupling then rotates $\mathbf{K}_{sr}$ into the field-dressed hyperfine basis that diagonalizes the long-range Hamiltonian. In the limit that the hyperfine and Zeeman splittings vanish, the frame transformation becomes essentially exact, limited only by the quality of the energy-analytic reference functions. We consider two variations of the frame transformation: (1) the energy-independent frame transformation (EIFT), which

---

[*]Current address: Department of Physics, University of Illinois Chicago, Chicago, Illinois 60607, USA; alasko5@uic.edu

[†]nmehta@trinity.edu

requires only the zero-energy quantum defects to compute $\mathbf{K}_{sr}$, and (2) the energy-dependent frame transformation (EDFT), which requires the quantum defects on a course grid of energy spanning the separation of two-body collision thresholds determined by the hyperfine-Zeeman energies.

A number of studies [23–25] have utilized an energy-independent frame transformation to build essentially a three-parameter MQDT that requires only the singlet and triplet scattering lengths $a_S$ and $a_T$, and the leading dispersion coefficient $C_6$. In such a scheme, $a_S$, $a_T$, and $C_6$ may be considered tunable parameters that can be adjusted to reproduce low-energy observables such as the positions of certain Feshbach resonances. The simplicity of this approach gives it enormous predictive power, as demonstrated by a recent study that identified a very large number of "broad" Feshbach resonances [25]. The present study places such frame transformation calculations in context by providing direct comparisons to more accurate implementations of MQDT, and also to numerically converged coupled channels calculations, which we take here to be "exact."

This paper is structured as follows. In Sec. II, we discuss our model of alkali collisions, including the interaction Hamiltonian and field-dressed hyperfine-Zeeman basis. We describe the various Born-Oppenheimer potentials adapted for this work, discussing their properties and any necessary modifications made for the present calculations. Section III provides a brief overview of MQDT for ultracold collisions along with explanations of EIFT and EDFT. Our results, including the positions of $s$-wave resonance and zero crossings for particular collision channels of each species, are presented in Sec. IV.

We show that when one obtains $\mathbf{K}_{sr}$ from a rigorous boundary condition on a multichannel short-ranged solution—what we shall refer to as the "MQDT" calculation, the low-energy scattering observables agree, nearly exactly, with converged coupled-channels (CC) calculations using Johnson's log-derivative propagator [26]. The agreement between MQDT and CC calculations, however, is only possible if the model potential-energy functions for the singlet and triplet configurations reliably converge to the long-range dispersion form (5) at separation distances where all collision channels are locally open. We also find that frame transformation approximations for $\mathbf{K}_{sr}$ provide an excellent description of lighter alkali species, especially lithium, but become progressively unreliable for heavier species in which the hyperfine-Zeeman splitting is much larger, and the energy-dependence of the quantum defects over the necessary range of energy is appreciable.

Finally, it is worth mentioning that, while analytical solutions to the Schrödinger equation for potentials that vary as $R^{-6}$ have been formulated by Gao [17], we opt instead to use of the numerical approach proposed in Ref. [27], namely the Milne phase amplitude method [28], to compute the energy-analytic reference functions that play a key role in MQDT. This approach is, for our purpose, simpler and more versatile since it is applicable to the case of a more general long-range potential that includes higher-order dispersion terms—including these long-range dispersion terms reduces the energy dependence of the quantum defects and generally improves the MQDT. It is also, in our modest view, simpler to

implement than the rather complicated analytical solution of Ref. [17].

To a new student of MQDT, the literature can be daunting. In the process of this work, we have relied heavily on Refs. [22,29] to gain an understanding of MQDT methods, particularly as they relate to ultracold atomic collisions. The Appendix of Ref. [30] provides useful expressions for matrix elements relevant to the hyperfine-Zeeman Hamiltonian, and Ref. [27] provides a good starting point for computing the energy-analytic reference functions.

## II. MODEL OF ALKALI COLLISIONS

Our model for ultracold collisions of alkali atoms follows closely that of Ref. [31]. For two-body atomic scattering, one generally writes the wave function as $\Psi(R, \Omega) = R^{-1} \sum_i \psi_i(R) \Phi_i(\Omega)$, where $R$ is the nuclear separation of the atoms and $\Omega$ is a collective coordinate describing all angular and internal degrees of freedom. The problem is reduced to a coupled channels equation of the form

$$\sum_j \left[ \frac{\hbar^2}{2\mu} \left( -\frac{d^2}{dR^2} + \frac{\ell_j(\ell_j + 1)}{R^2} \right) \delta_{ij} + V_{ij} \right] \psi_j = E \psi_i. \quad (1)$$

Here, $\mu$ is the reduced mass of the homonuclear dimer. The interaction matrix $\mathbf{V}(R)$ for two ultracold alkali atoms in a magnetic field is of the form

$$\mathbf{V}(R) = \mathbf{P}_0 V_0(R) + \mathbf{P}_1 V_1(R) + \sum_{n=1}^{2} \mathbf{H}_n^{\text{HZ}}, \quad (2)$$

where $\mathbf{P}_0$ and $\mathbf{P}_1$ are the singlet and triplet projection operators, and $V_S(R)$ are the Born Oppenheimer potentials corresponding to the singlet ($S = 0$) and triplet ($S = 1$) molecular ground states $X\,^1\Sigma_g^+$ and $a\,^3\Sigma_u^+$, respectively. The matrix operator $\mathbf{H}_n^{\text{HZ}}$ is the combined hyperfine and Zeeman interaction for each atom,

$$\mathbf{H}_n^{\text{HZ}} = \left[ \frac{A_n}{\hbar^2} \vec{\mathbf{s}}_n \cdot \vec{\mathbf{i}}_n + \frac{\mu_B}{\hbar} (g_s \vec{\mathbf{s}}_n + g_{ni} \vec{\mathbf{i}}_n) \cdot \vec{B} \right], \quad (3)$$

where $\vec{\mathbf{i}}_n$ and $\vec{\mathbf{s}}_n$ are the nuclear and electronic spins of atom $n$, $A_n$ is the hyperfine coupling in the electronic ground state, and $g_s$ and $g_{ni}$ are electron and nuclear $g$-factors in units of the bohr magneton $\mu_B$. We adhere to the convention of Ref. [32] and define the $g$ factors to be of the opposite sign as their corresponding magnetic dipole moments. For convenience and clarity, a collection of the relevant parameters from Ref. [32] is given in Table I.

The two-atom collision thresholds in a magnetic field are determined by the eigenstates of $\mathbf{V}(R)$ in the limit $R \to \infty$, where $V_S(R)$ vanishes. These states are constructed by appropriately symmetrizing the eigenstates of Eq. (3). The hyperfine interaction couples the nuclear spin $\vec{\mathbf{i}}$ and electronic spin $\vec{\mathbf{s}}$ of each atom and is diagonal in the total atomic spin $\vec{\mathbf{f}} = \vec{\mathbf{i}} + \vec{\mathbf{s}}$. However, the Zeeman interaction couples states of different $f$, so that only the projection $m_f$ remains a good quantum number at finite field. While the states of $\mathbf{H}_n^{\text{HZ}}$ can be found analytically by the Breit-Rabi formula [33]—for a detailed derivation, see Ref. [34]—in practice, we compute the matrix elements of the Hamiltonian in Eq. (3) in the

TABLE I. Hyperfine couplings and nuclear $g$ factors used in this work. Nuclear $g$ factors $g_i$ should be multiplied by the bohr magneton.

| Atom | $i$ | $g_i$ | $A_{\text{hf}}/h$[MHz] |
|------|-----|-------|------------------------|
| $^6$Li | 1 | $-0.000\,447\,654\,0(3)$ | $152.136\,840\,7(20)$ |
| $^7$Li | 3/2 | $-0.001\,182\,213(6)$ | $401.752\,043\,3(5)$ |
| $^{23}$Na | 3/2 | $-0.000\,804\,610\,8(8)$ | $885.813\,064\,4(5)$ |
| $^{39}$K | 3/2 | $-0.000\,141\,934\,89(12)$ | $230.859\,860\,1(3)$ |
| $^{40}$K | 4 | $+0.000\,176\,490\,(34)$ | $-285.7308(24)$ |
| $^{85}$Rb | 5/2 | $-0.000\,293\,640\,0(6)$ | $1011.910\,813(2)$ |
| $^{87}$Rb | 3/2 | $-0.000\,995\,141\,4(10)$ | $3417.341\,306\,42(15)$ |
| $^{133}$Cs | 7/2 | $-0.000\,398\,853\,95(52)$ | $2298.157\,942\,5$ |

hyperfine basis $|f, m_f\rangle$ and diagonalize the resulting matrix numerically. Figure 1 shows the energy levels of a single atom in a magnetic field for all of the alkali species considered here except for $^{40}$K, which has a negative hyperfine coupling constant that results in the inverted diagram shown in Fig. 2. As we discuss below, these energies will determine the two-atom collision thresholds.

The short-ranged physics ($R \lesssim 30a_0$) of Eq. (2) is dominated by the very deep singlet and triplet potentials, while the long-range physics ($R \gtrsim 30a_0$) is controlled by the comparatively shallow van der Waals tail and weak hyperfine-Zeeman structure of the atoms. For $R \gtrsim 30a_0$, the off-diagonal elements of $V_{ij}(R)$ in Eq. (1) vanish, and the diagonal elements
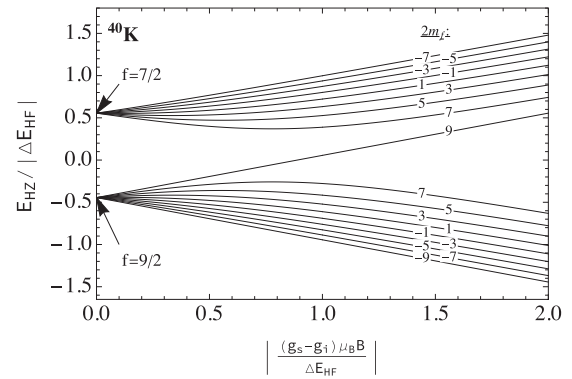


FIG. 2. The one-atom Breit-Rabi energy spectrum for $^{40}$K, for which the hyperfine coupling is negative, leading to an inverted Breit-Rabi diagram.

are determined by the dispersion coefficients $C_6$, $C_8$, and $C_{10}$:

$$V_{ii}(R) - E_i^{\text{th}} \rightarrow V_{\text{LR}}(R), \tag{4}$$

where $E_i^{\text{th}}$ are the collision thresholds and the long-range potential common to all channels is of the form

$$V_{\text{LR}}(R) = -\frac{C_6}{R^6} - \frac{C_8}{R^8} - \frac{C_{10}}{R^{10}} \text{ for } R \gtrsim 30a_0. \tag{5}$$

The natural unit of length $\beta$ associated with $V_{\text{LR}}$, and the corresponding natural unit of energy $E_\beta$ are fixed by the depth
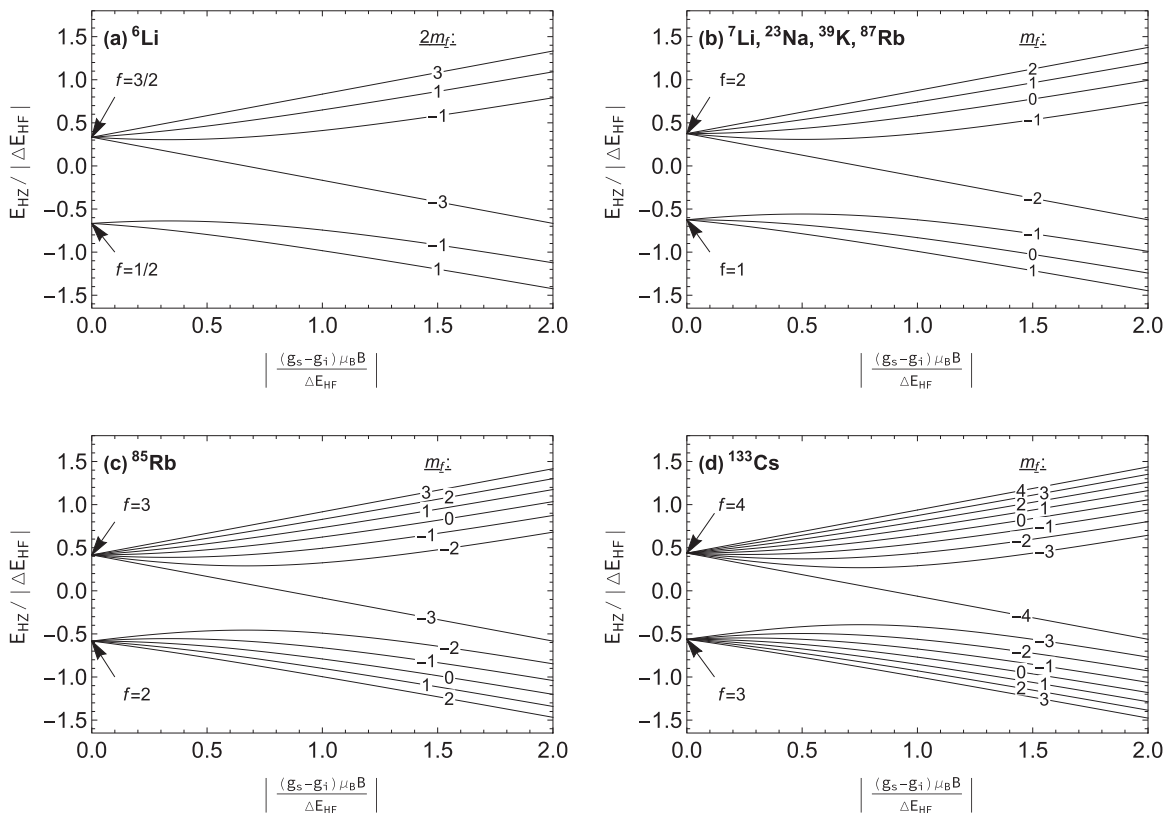


FIG. 1. The one-atom Breit-Rabi energy spectrum for atomic species considered in this work. The $f$ quantum number is only good in the zero-field limit. At any field, $m_f$ remains a good quantum number, but different $f$ levels are coupled. The curves are labeled by their $m_f$ quantum number, or in cases where $m_f$ is fractional, by $2m_f$.

of $V_{\text{LR}}$ at a separation distance $\beta$:

$$E_\beta = \frac{\hbar^2}{2\mu\beta^2} = |V_{\text{LR}}(\beta)|. \qquad (6)$$

This definition reduces to twice the usual van der Waals length when $C_8 = C_{10} = 0$, $\beta_6 = (2\mu C_6/\hbar^2)^{1/4} = 2R_{\text{vdW}}$ and renders the dispersion coefficients unitless when expressed in these units.

### A. Field-dressed hyperfine basis

For the two-atom system, we follow Ref. [31] and represent the symmetry requirements for identical bosons or fermions by defining the basis kets as

$$|\{\alpha\beta\}\rangle = \frac{|\alpha,\beta\rangle \pm (-1)^\ell |\beta,\alpha\rangle}{\sqrt{2(1+\delta_{\alpha,\beta})}}, \qquad (7)$$

where the Greek letters refer to the internal states of the individual atoms. For example, $|\alpha,\beta\rangle = |f_1,m_1,f_2,m_2\rangle$ represents atom 1 in hyperfine state $|\alpha\rangle = |f_1,m_1\rangle$ and atom 2 in state $|\beta\rangle = |f_2,m_2\rangle$, while the $+$ $(-)$ sign is taken for bosons (fermions). We neglect in this work the magnetic dipole-dipole interaction, so the $s$ wave remains decoupled from higher partial waves. Furthermore, the total $M_F = m_{f_1} + m_{f_2}$ remains a good quantum number at finite field. Each calculation presented here is specified by a particular $M_F$, within which the lowest one-atom states can be read by the Breit-Rabi graphs.

The properly symmetrized eigenstates of the two-atom hyperfine-Zeeman Hamiltonian comprise the "field-dressed" basis, constructed as a linear combination of symmetrized atomic hyperfine states

$$|i\rangle = \sum_{\{\alpha\beta\}} C^i_{\{\alpha\beta\}} |\{\alpha\beta\}\rangle. \qquad (8)$$

The scattering thresholds correspond to the elements of the diagonal matrix

$$\mathbf{E}_{\text{th}} = \mathbf{C}^{\text{T}}(B)\mathbf{H}^{\text{HZ}}\mathbf{C}(B), \qquad (9)$$

where $\mathbf{C}(B)$ is the field-dependent rotation comprised of the eigenvector elements $C^i_{\{\alpha\beta\}}$. We express and solve Eq. (1) in the field-dressed spin basis given by Eq. (8).

The scattering cross section is determined by matching the solutions to asymptotic Bessel functions in the limit $R \to \infty$. In our calculations, because we neglect the weak, long-ranged magnetic dipole-dipole interaction, we match at a radius $R$ much larger than the natural length $\beta$, where both the singlet $V_0(R)$ and triplet $V_1(R)$ potentials become negligible, and the two-atom interaction is reduced to a sum of one-atom terms: $\lim_{R\to\infty} \mathbf{V}(\mathbf{R}) = \mathbf{H}^{\text{HZ}} = \sum_{n=1}^2 \mathbf{H}_n^{\text{HZ}}$. In practice, $R \approx 20\beta$ is sufficiently large to ensure that the van der Waals tail is negligible. We consider only $s$-wave collisions in this work, but a larger matching radius may be necessary for higher partial waves, particularly at threshold energies.

### B. Singlet and triplet potentials

A great deal of effort has been expended by many authors [35–46] in the development of state-of-the-art Born-Oppenheimer potential curves for alkali dimers in the spin
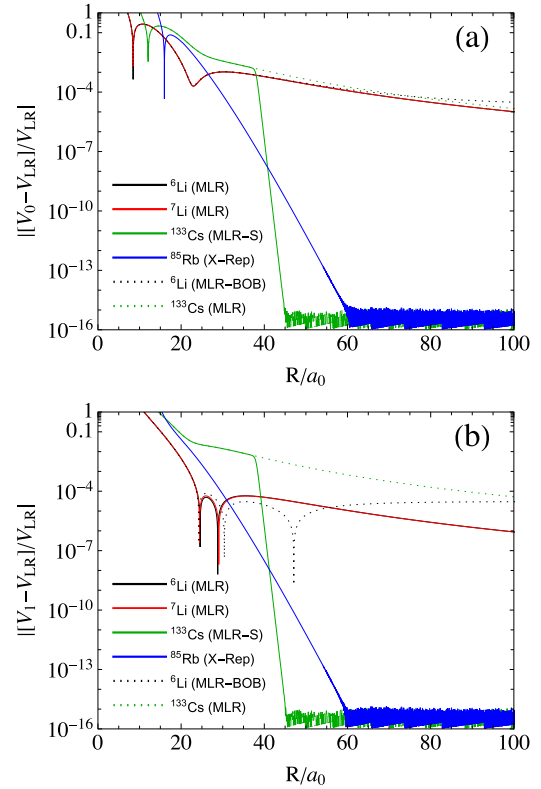


FIG. 3. Convergence of the singlet and triplet potentials to their asymptotic form is shown for a few illustrative cases. Panel (a) shows the singlet potentials while panel (b) shows the triplet potentials. The solid lines correspond to potentials as they are used in this work, while the dotted curves represent unaltered potentials for $^6$Li (dotted black) and for $^{133}$Cs (dotted green).

singlet ($X\,^1\Sigma_g^+$) and spin triplet ($a\,^3\Sigma_u^+$) configurations. The models we adopt here were chosen because they are given in closed analytic form with conveniently tabulated parameters. The models broadly fall into two categories: (1) the Hannover polynomial expansion (or X-representation) [35,36], and (2) the Morse–Long-Range (MLR) potential [37,38]. Details regarding these models are contained in Refs. [39–44].

The Hannover X-Rep potentials are used for $^{23}$Na [41], $^{39}$K [42], $^{40}$K [42], $^{85}$Rb [43], and $^{87}$Rb [43]. These potentials require essentially no modification for our purpose; they allow for immediate and direct comparisons with experimentally observed Feshbach resonance positions. Moreover, these potentials exhibit rapid exponential convergence to the asymptotic form $V_{\text{LR}}$ of Eq. (5) for $R \gtrsim 30a_0$. The long-range form of the potentials in the X-representation is of the form

$$V_S^{(\text{X-Rep})}(R) \to V_{\text{LR}}(R) \pm A_{\text{ex}}R^\gamma e^{-\beta_{\text{ex}}R}. \qquad (10)$$

When including the exponential "exchange" term, we take the "+" sign for the triplet and the "−" sign for the singlet. In Fig. 3, we show the relative error of the singlet [Fig. 3(a)] and triplet [Fig. 3(b)] potentials with respect to the long-range potential $V_{\text{LR}}$ for a selection of alkali dimers. The X-Rep potential is shown only for the case of $^{85}$Rb, but other potentials of this type exhibit similar convergence.

The MLR potentials used for $^6$Li, $^7$Li, and $^{133}$Cs, on the other hand, do not behave asymptotically as Eq. (10)

[39,40,44]. While they do indeed converge to the form of Eq. (5), that convergence is significantly slower than the exchange term, as seen by the red $^7$Li curve in Fig. 3. The MLR potentials for $^6$Li also include so-called "Born-Oppenheimer breakdown" (BOB) corrections, which are not included in the potentials for the "reference" isotopologue $^7$Li$_2$. These corrections are configuration-dependent. They behave as $R^{-6}$ to leading order and alter the long-range potential, leading to an "effective" $C_6$ coefficient that is different for the singlet and triplet configurations. Therefore, neither of the potentials for $^6$Li converge to $V_{\mathrm{LR}}$, as demonstrated by the dotted-black curves in Fig. 3. Meanwhile, the MLR potentials for $^{133}$Cs exhibit even slower convergence to $V_{\mathrm{LR}}$, particularly for the triplet, as shown by the dotted-green curve in Fig. 3. We shall soon discuss how these potentials are modified in this work in order to accommodate an MQDT treatment, which requires that the boundary condition for determining $\mathbf{K}_{\mathrm{sr}}$ be applied at a separation distance where (1) the off-diagonal elements of $V_{ij}$ vanish, and (2) the diagonal elements $V_{ii}$ are reliably converged to $V_{\mathrm{LR}}$ while and all collision channels are locally open.

For potentials of the Hannover X-Rep type, the matching radius $R_m$ at which $\mathbf{K}_{\mathrm{sr}}$ is determined may be chosen to be as small as $30a_0$, and all quantum defects are independent of this matching radius up to about $R_m \approx 40a_0$ where some collision channels begin to become energetically closed. For potentials of the MLR type, however, the convergence to the asymptotic form is prohibitively slow, and two options are available for improving the performance of both MQDT and FT methods. First, one may extend the matching radius out beyond the distance at which all channels are strictly open at the risk of incurring greater energy dependence in the quantum defects. Second, one may *force* the singlet and triplet potentials to the long-range form by using a "switching" function like Eq. (46). We take the former strategy with lithium where the hyperfine-Zeeman splitting is relatively weak, and even at separation distances of $55a_0$, the quantum defects vary smoothly, nearly linearly with energy. For cesium, however, the higher collision channels are strongly closed beyond about $40a_0$ and the energy dependence in $\mathbf{K}_{\mathrm{sr}}$ and $\mu_S$ quickly becomes unmanageable, so we take the latter strategy and force $V_S^{\mathrm{MLR}} \to V_{\mathrm{LR}}$ for $R \gtrsim 40a_0$. As discussed above, the Born-Oppenheimer breakdown corrections [39,40] included in the MLR potentials for $^6$Li produce different "effective" $C_6$ coefficients for the singlet and triplet configurations. This is undesirable for an MQDT calculation, and so we have chosen to exclude these corrections from the potential. We have replaced the dispersion coefficients quoted in Refs. [39,40] with those of Ref. [47], which include nonadiabatic corrections as well. For a comprehensive list of dispersion coefficients used in this work, see Table II. This replacement significantly changes the singlet and triplet scattering lengths, and further changes to the potential are necessary in order to restore $a_S$ and $a_T$ to more realistic values. A common strategy [48,57] for reproducing experimental data is to adjust the volume of the potentials by adding a quadratic term inside the equilibrium distance (i.e., for $R < R_e$ where $R_e$ is the potential energy minimum) of the form

$$V_{\mathrm{shift}}(R) = V_c^{(S)}(R - R_e)^2 \text{ for } R < R_e. \quad (11)$$

TABLE II. Dispersion coefficients used in this work.

| Dimer | Ref. | $C_6[E_h a_0^6]$ | $C_8[E_h a_0^8]$ | $C_{10}[E_h a_0^{10}]$ |
|---|---|---|---|---|
| $^6$Li$_2$ | [47] | 1394.1608 | $8.346\,030\,6 \times 10^4$ | $7.374\,489\,5 \times 10^6$ |
| $^7$Li$_2$ | [47] | 1394.0508 | $8.345\,586\,0 \times 10^4$ | $7.374\,198\,4 \times 10^6$ |
| $^{23}$Na$_2$ | [41] | 1560.0791 | $1.249\,611\,3 \times 10^5$ | $8.155\,141\,1 \times 10^6$ |
| $^{39}$K$_2$ | [42] | 3925.9127 | $4.223\,789\,7 \times 10^5$ | $4.937\,959\,1 \times 10^7$ |
| $^{40}$K$_2$ | [42] | 3925.9127 | $4.223\,789\,7 \times 10^5$ | $4.937\,959\,1 \times 10^7$ |
| $^{85}$Rb$_2$ | [43] | 4710.2163 | $5.766\,964\,5 \times 10^5$ | $7.591\,280\,9 \times 10^7$ |
| $^{87}$Rb$_2$ | [43] | 4710.2163 | $5.766\,964\,5 \times 10^5$ | $7.591\,280\,9 \times 10^7$ |
| $^{133}$Cs$_2$ | [44] | 6881.3838 | $1.022\,55 \times 10^6$ | $1.5903 \times 10^8$ |

Here, $V_c^{(S)}$ are constant parameters that may be adjusted to reproduce the desired scattering lengths (or particular resonance positions) and $S$ is the total spin quantum number.

Table III shows our scattering length calculations for all of the alkali species considered in this work. Despite the fact that the computation of single-channel scattering lengths is a relatively simple, numerically stable procedure– - at least compared with solutions to large coupled channels problems—our calculations yield scattering lengths different from other published values for the same potentials. The differences are slight, yet significant since the precise positions of magnetic Feshbach resonances are sensitive to small changes in the singlet and triplet phase shifts. These differences are discussed case-by-case in Sec. IV.

## III. MULTICHANNEL QUANTUM DEFECT THEORY FOR ULTRACOLD COLLISIONS

As discussed in Sec. II, the two-atom Hamiltonian exhibits a natural separation of energy and length scales. At short-range ($R \lesssim 30a_0$), the interaction is dominated by the deep singlet and triplet potentials, while at longer range $R \gtrsim 30a_0$, the potentials approach their comparatively weak long-range dispersion form Eq. (5), offset by thresholds determined by the two-atom hyperfine-Zeeman interaction. At asymptotically large distances $R \gg \beta$, the solution may be matched to Bessel functions to determine the physical $K$ matrix. The basic MQDT procedure is as follows: (1) Solve the Schrödinger equation in each of these three regions, the short-range region, the van der Waals, and the asymptotic region. (2) Match the short-ranged numerical solution to the solution in the van der Waals region in order to determine the short-range $K$ matrix $\mathbf{K}_{sr}$, whose eigenvalues exhibit smooth, simple dependence on energy and field. (3) Match the solution in the van der Waals region where all collision channels are locally open to the appropriate asymptotic solution in order to compute a physical $K$ matrix. Here, we shall focus on steps (2) and (3) of this procedure. For step (1), we use Johnson's log-derivative propagator [26].

### A. Overview of multichannel quantum-defect theory

Central to the implementation of MQDT, we seek a linearly independent pair of solutions, $\hat{f}_i(R)$ and $\hat{g}_i(R)$, to the single-channel Schrödinger equation in the presence of $V_{\mathrm{LR}}(R)$ that are analytic in energy across the collision threshold. These

TABLE III. Scattering lengths for alkali dimers.

| $X^1\Sigma_g^+/a^3\Sigma_u^+$ model | Present calculation | | | | Literature | | |
|---|---|---|---|---|---|---|---|
| | $V_c^0[E_h/a_0^2]$ | $V_c^1[E_h/a_0^2]$ | $a_S/a_0$ | $a_T/a_0$ | $a_S/a_0$ | $a_T/a_0$ | Other Refs. |
| $^6$Li$_2$ (MLR) [39,40] | $2.65 \times 10^{-7}$ | $1.25465 \times 10^{-06}$ | 45.166 | $-2121.11$ | 45.154(2) [48] | $-2113(2)$ [48] | [49,50] |
| $^7$Li$_2$ (MLR) [39,40] | $1.88 \times 10^{-6}$ | $1.85 \times 10^{-6}$ | 34.339 | $-26.923$ | 34.331(2) [48] | $-26.92(7)$ [48] | [50] |
| $^{23}$Na$_2$ (X-rep) [41] | 0 | 0 | 18.820 | 64.302 | 18.81(80) [41] | 64.30(40) [41] | [51,52] |
| $^{39}$K$_2$ (X-rep) [42] | 0 | 0 | 138.808 | $-33.391$ | 138.80 [42] | $-33.41$ [42] | [53] |
| $^{40}$K$_2$ (X-rep) [42] | 0 | 0 | 104.425 | 169.185 | 104.42 [42] | 169.18 [42] | [53] |
| $^{85}$Rb$_2$ (X-rep) [43] | 0 | 0 | 2572.37 | $-392.496$ | 2720 [43] | $-386.9$ [43] | [54,55] |
| $^{87}$Rb$_2$ (X-rep) [43] | 0 | 0 | 90.161 | 98.867 | 90.35 [43] | 99.04 [43] | [55] |
| $^{133}$Cs$_2$ (MLR) [44] | $-2.53 \times 10^{-7}$ | $5.9705 \times 10^{-7}$ | 280.253 | 2405.21 | 280.25 [44] | 2405.6 [44] | [56,57] |

reference functions satisfy

$$\left(\frac{\hbar^2}{2\mu}\left[-\frac{d^2}{dR^2} + \frac{l_i(l_i+1)}{R^2}\right] + V_{LR}(R) - E_i\right)$$
$$\times \left\{\hat{f}_i(R) \ \hat{g}_i(R)\right\} = 0, \qquad (12)$$

with $E_i = E - E_i^{\text{th}}$. The desired reference functions are constructed using the Milne phase amplitude method [27,28]:

$$\hat{f}_i(R) = \alpha_i(R)\sin\left(\int_{R_x}^{R}\alpha_i^{-2}(R')dR' + \phi_i\right), \qquad (13)$$

$$\hat{g}_i(R) = -\alpha_i(R)\cos\left(\int_{R_x}^{R}\alpha_i^{-2}(R')dR' + \phi_i\right), \qquad (14)$$

where $\phi_i$ is a channel-dependent (but energy-*independent*) phase and $\alpha_i(R)$ satisfies the nonlinear differential equation

$$\alpha_i(R)'' + k_i^2(R)\alpha_i(R) = \alpha_i^{-3}(R). \qquad (15)$$

Here, $k_i(R) = \{2\mu[E_i - V_{LR}(R)]/\hbar^2 - \ell_i(\ell_i+1)/R^2\}^{1/2}$ is the local wave number in the $i$th channel. It is convenient to impose Wenzel-Kramers-Brillouin–like (WKB-like) boundary conditions [27] deep in the well (we choose $R_x = 0.07\beta$) of the long-range reference potential:

$$\alpha_i(R_x) = \frac{1}{\sqrt{k_i(R_x)}}, \qquad (16)$$

and

$$\alpha_i'(R_x) = \frac{d}{dR}\left(\frac{1}{\sqrt{k_i(R)}}\right)_{R=R_x}. \qquad (17)$$

The selection of the point $R_x$ in Eqs. (14)–(17) is somewhat arbitrary. All that is required is that $V_{LR}$ is deep enough that our semiclassical boundary conditions are reasonable.

Fixing the energy-independent phase $\phi_i$ in Eq. (14) amounts to a "standardization" of the MQDT reference functions, ensuring that their asymptotic form is largely universal for all potentials of the form (5) that approach $-C_6/R^6$ in the limit $R \to \infty$. The strategy is to focus on the zero-energy solutions to the $-C_6/R^6$ potential [22,29],

$$\chi_0^+(R) = \sqrt{\frac{R}{\beta}}J_{-\frac{1}{4}(2\ell+1)}\left(\frac{\beta^2}{2R^2}\right), \qquad (18)$$

$$\chi_0^-(R) = \sqrt{\frac{R}{\beta}}J_{\frac{1}{4}(2\ell+1)}\left(\frac{\beta^2}{2R^2}\right), \qquad (19)$$

where $J_\nu(x)$ is the Bessel function of the first kind. As $R \to \infty$, $\chi_0^+ \propto R^{\ell+1}$ and $\chi_0^- \propto R^{-\ell}$. One possible standardization is to choose the phase $\phi_i$ such that $\hat{f}_i(R)$ coincides with $\chi_0^+(R)$ as $R \to \infty$ [22]. However, for $l > 0$, this choice causes the reference functions to lose their linear independence since $\hat{g}_i(R)$ becomes a linear combination of $\chi_0^+(R)$ and $\chi_0^-(R)$, and consequently both $\hat{f}_i(R)$ and $\hat{g}_i(R)$ grow exponentially under the centrifugal barrier. To make our formulation easily adaptable to higher partial waves, we adhere to the standardization proposed in Ref. [29], demanding instead that $\hat{g}(R)$ coincide with $\chi_0^-$ at zero energy. There is a unique value of $\tan\phi_i$ that satisfies this condition [29], namely,

$$\tan\phi_i = -\left(\frac{W(\chi_0^-, \hat{g}_{i\phi_i=0})}{W(\chi_0^+, \hat{f}_{i\phi_i=0})}\right)_{R=R_f}, \qquad (20)$$

where $W(x, y)$ is the Wronskian and is given by $W(x, y) = x(R)y'(R) - x'(R)y(R)$ and $R_f = 20\beta$ is sufficiently large for the present study.

The linearly independent reference functions $\hat{f}_i(R)$ and $\hat{g}_i(R)$ are used to define the short-ranged $K$ matrix $\mathbf{K}_{sr}$ via a boundary condition on the general solution to Eq. (1) $\boldsymbol{\psi}(R)$ at $R_m$, somewhere in the van der Waals region. We let $\hat{\mathbf{f}}(R)$ and $\hat{\mathbf{g}}(R)$ be diagonal matrices in the field-dressed channel space with functions $\hat{f}_i(R)$ and $\hat{g}_i(R)$, respectively, along the diagonal. Then

$$\boldsymbol{\psi}(R) = \hat{\mathbf{f}}(R) - \hat{\mathbf{g}}(R)\mathbf{K}_{sr}. \qquad (21)$$

Here, $\boldsymbol{\psi}(R)$ is a matrix of solutions with elements $\psi_{i\beta}$, where $\beta$ denotes the state index, and $i$ denotes the channel component. At very large separation distance ($R \gtrsim 20\beta$), $V_{LR} \to 0$ and the atomic system is described by a set of uncoupled equations,

$$\left(\frac{\hbar^2}{2\mu}\left[-\frac{d^2}{dR^2} + \frac{\ell_i(\ell_i+1)}{R^2}\right] - E_i\right)\psi_i(R) = 0, \qquad (22)$$

where $E_i = E - E_i^{\text{th}}$. For open channels with $E_i > 0$, the solution $\psi_i(R)$ is given by a linear combination of phase-shifted Riccati functions which asymptotically behave as

$$f_i(R) \to \sqrt{\frac{2\mu}{\pi k_i \hbar^2}}\sin\left(k_i R - l_i\frac{\pi}{2} + \eta_i\right), \qquad (23)$$

$$g_i(R) \to -\sqrt{\frac{2\mu}{\pi k_i \hbar^2}}\cos\left(k_i R - l_i\frac{\pi}{2} + \eta_i\right), \qquad (24)$$

as $R \to \infty$. The parameter $\eta_i$ represents the phase that is accumulated in the van der Waals region and is given by

$$\tan \eta_i = \left( \frac{W(\hat{f}_i(R), f_i^s(R))}{W(\hat{f}_i(R), g_i^s(R))} \right)_{R=R_f}. \qquad (25)$$

Here $f_i^s(R)$ and $g_i^s(R)$ are the Riccati functions which approach

$$f_i^s(R) \to \sqrt{\frac{2\mu}{\pi k_i \hbar^2}} \sin \left( k_i R - l_i \frac{\pi}{2} \right), \qquad (26)$$

$$g_i^s(R) \to -\sqrt{\frac{2\mu}{\pi k_i \hbar^2}} \cos \left( k_i R - l_i \frac{\pi}{2} \right). \qquad (27)$$

The "energy-normalized reference functions" given in Eqs. (23) and (24) $\{f_i, g_i\}$ are related to $\{\hat{f}_i, \hat{g}_i\}$ by the following transformation:

$$\begin{pmatrix} f_i \\ g_i \end{pmatrix} = \begin{pmatrix} \mathcal{A}_i^{1/2} & 0 \\ \mathcal{A}_i^{-1/2}\mathcal{G}_i & \mathcal{A}_i^{-1/2} \end{pmatrix} \begin{pmatrix} \hat{f}_i \\ \hat{g}_i \end{pmatrix}, \qquad (28)$$

where the parameter $\mathcal{A}_i$ is related to the energy-normalization of $\{f_i, g_i\}$ and $\mathcal{G}_i$ accounts for the phase difference accumulated by $\{\hat{f}_i, \hat{g}_i\}$ in $V_{LR}$ [29]. These parameters are computed using the following formulas:

$$\mathcal{A}_i = -\left( \frac{W(\hat{g}_i, f_i^s) - \tan \eta_i W(\hat{g}_i, g_i^s)}{W(\hat{f}_i, g_i^s) + \tan \eta_i W(\hat{f}_i, f_i^s)} \right)_{R=R_f}, \qquad (29)$$

$$\mathcal{G}_i = -\left( \frac{W(\hat{g}_i, g_i^s) + \tan \eta_i W(\hat{g}_i, f_i^s)}{W(\hat{f}_i, g_i^s) + \tan \eta_i W(\hat{f}_i, f_i^s)} \right)_{R=R_f}. \qquad (30)$$

For closed channels $(E_i < 0)$, the solution is a superposition of $\hat{f}_i(R)$ and $\hat{g}_i(R)$ that vanishes as $R \to \infty$:

$$\hat{f}_i(R) + \cot \gamma_i \hat{g}_i(R) \to \propto e^{-\kappa_i R}. \qquad (31)$$

Here, $\kappa_i = (2\mu |E_i|/\hbar^2)^{1/2}$ and $\gamma_i$ is a parameter that determines what combination of $\{\hat{f}_i, \hat{g}_i\}$ vanishes as $R \to \infty$. It is computed by

$$\tan \gamma_i = \left( \frac{W(e^{-\kappa_i r}, \hat{g}_i(R))}{W(e^{-\kappa_i r}, \hat{f}_i(R))} \right)_{R=R_f}. \qquad (32)$$

With the energy-dependent MQDT parameters $\mathcal{A}$, $\mathcal{G}$, and $\cot \gamma$ in hand, one may determine the $K$-matrix defining the asymptotic boundary condition with respect to functions $f_i(R)$ and $g_i(R)$, namely, $\psi(R) \to \mathbf{f} - \mathbf{g} \mathbf{K}$. First, $\mathbf{K}_{sr}$ is partitioned into blocks depending on which channels are asymptotically opened $(P)$ or closed $(Q)$:

$$\mathbf{K}_{sr} = \begin{pmatrix} K_{PP}^{sr} & K_{PQ}^{sr} \\ K_{QP}^{sr} & K_{QQ}^{sr} \end{pmatrix}. \qquad (33)$$

Then, we use the closed-channel parameter $\gamma$ to transform the $N \times N$ short-range reaction matrix into an $N_P \times N_P$ matrix using the channel-closing formula

$$\tilde{\mathbf{K}} = \mathbf{K}_{PP}^{sr} - \mathbf{K}_{PQ}^{sr} (\mathbf{K}_{QQ}^{sr} + \cot \boldsymbol{\gamma})^{-1} \mathbf{K}_{QP}^{sr}. \qquad (34)$$

This transformation accounts for the reflected amplitude arising from closed channels, and captures the physics of

closed-channel resonances. Next, $\tilde{\mathbf{K}}$ must be properly normalized with respect to energy. This is accomplished with the expression,

$$\mathbf{K} = \mathcal{A}^{1/2} \tilde{\mathbf{K}} (1 + \mathcal{G}\tilde{\mathbf{K}})^{-1} \mathcal{A}^{1/2}. \qquad (35)$$

This $\mathbf{K}$, however, is not yet the full physical $K$ matrix because it does not include effects from the additional phase $\eta$ which $\{f, g\}$ acquire with respect to $\{f^s, g^s\}$. We obtain a physical $S$ matrix by

$$\mathbf{S}^{\mathrm{phys}} = e^{i\eta} \frac{1 + i\mathbf{K}}{1 - i\mathbf{K}} e^{i\eta}, \qquad (36)$$

from which $\mathbf{K}^{\mathrm{phys}}$ is obtained by

$$\mathbf{K}^{\mathrm{phys}} = i \frac{1 - \mathbf{S}^{\mathrm{phys}}}{1 + \mathbf{S}^{\mathrm{phys}}}. \qquad (37)$$

Note that, in the above expressions, $\boldsymbol{\gamma}$, $\mathcal{A}$, $\mathcal{G}$, and $\boldsymbol{\eta}$ are diagonal matrices of the corresponding MQDT functions evaluated at the appropriate channel energy $E - E_i^{\mathrm{th}}$.

For ultracold collisions in the lowest channel, $\tilde{\mathbf{K}}$, $\mathbf{K}$, and $\mathbf{K}^{\mathrm{phys}}$ are each reduced to a single matrix element, and one can write the physical $K$-matrix element as

$$K^{\mathrm{phys}} = \frac{\tan \eta + K}{1 - K \tan \eta}, \qquad (38)$$

or in terms of the *s*-wave phase shift as

$$K^{\mathrm{phys}} = \tan \delta. \qquad (39)$$

We are primarily interested in the scattering length $a$, which is related to the *s*-wave phase shift $\delta$ by

$$a = -\lim_{k \to 0} \frac{\tan \delta}{k}. \qquad (40)$$

In all calculations presented here, we compute the MQDT functions using Eqs. (25), (29), (30), and (32).

### B. Frame transformation

At short separation distances, i.e., $R \lesssim 30a_0$, the physics is dominated by the deep Born-Oppenheimer potentials $V_S(R)$. Therefore, to a good approximation, any hyperfine or Zeeman interactions can be neglected at short range, and the atomic system can be described by a set of uncoupled equations in the singlet and triplet channels written here only for the *s*-wave,

$$\left( -\frac{\hbar^2}{2\mu} \frac{d^2}{dR^2} + V_S(R) - E \right) \psi_S(R) = 0. \qquad (41)$$

In Fig. 4 we show the quantum defects $\mu_S(E)$ in the singlet and triplet eigenchannels as a function of energy. The range of energy is different for each dimer and is determined by the maximum energy difference between collision thresholds $\Delta E^{\mathrm{th}} = \max E_i^{\mathrm{th}} - \min E_i^{\mathrm{th}}$ at the largest fields considered, 1200 G. For collisions at energies near the lowest threshold $(\min E_i^{\mathrm{th}})$, there may be a resonance due to a bound state attached to the highest threshold $(\max E_i^{\mathrm{th}})$ so the lowest energy one may imagine evaluating the quantum defect at is $-\Delta E^{\mathrm{th}}$. Meanwhile, one may imagine collisions of atoms prepared in excited magnetic levels undergoing collisions that occur at relatively high energy $(\Delta E^{\mathrm{th}})$ with respect to the ground-state
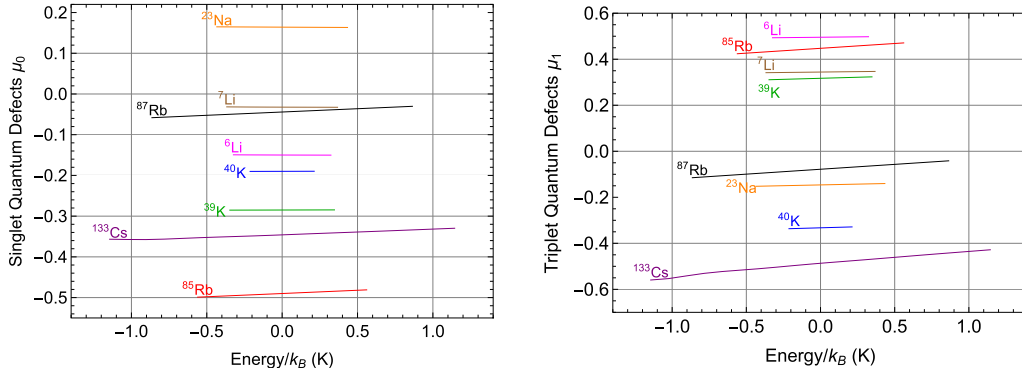
FIG. 4. Quantum defects for both the singlet (left) and triplet (right) potential-energy functions are shown for each homonuclear dimer. The energy (divided by the Boltzmann constant, $k_B$) scale is given in kelvin. The range of energies for each case is fixed by the maximum separation of collision thresholds, ranging from $-|\Delta E^{\mathrm{th}}|$ to $+|\Delta E^{\mathrm{th}}|$, where $\Delta E^{\mathrm{th}} = \max E_i^{\mathrm{th}} - \min E_i^{\mathrm{th}}$ at the largest fields considered (1200 G).

channel. These collisions are not explicitly considered in this work but nevertheless suggest that one requires the quantum defects, in principle, over a range $-|\Delta E^{\mathrm{th}}| < E < |\Delta E^{\mathrm{th}}|$. More technically, the scale $\Delta E^{\mathrm{th}}$ is set by an EDFT calculation, which requires that we compute the channel-weighted average energy Eq. (44). As one varies atomic mass from $^6$Li to $^{133}$Cs, one finds that $\Delta E^{\mathrm{th}}$ varies also from $\approx 0.25$ K $\approx$ 5 GHz to about $\approx 1$ K $\approx$ 20 GHz. Over the scale of relevant energies, the defects themselves vary roughly linearly, with slopes tending roughly to increase with mass.

To find the solution $\psi_S(R)$, we numerically integrate Eq. (41) from $R \approx a_0$, sufficiently small so that $\psi(R) \to 0$ due to the hard repulsive core of the potential, out to $R_m \sim 40a_0$ (or $55a_0$ for lithium as described in Sec. II B). Then we match each solution to a linear combination of $\hat{f}(R)$ and $\hat{g}(R)$ at $R_m$ to determine the singlet and triplet quantum defects $\mu_S$ at zero energy. These *single-channel* quantum defects are determined by imposing a single channel boundary condition [analogous to Eq. (21)] on the numerical solution $\psi_S(R)$ to Eq. (41),

$$\psi_S(R) \to \hat{f}(R) - \hat{g}(R) \tan(\pi \mu_S). \tag{42}$$

At large $R$, however, the total electronic spin $S$ is no longer a good quantum number and the interaction between the particles is no longer diagonal in the molecular basis $|\lambda\rangle = |SM_SIM_I\rangle$. The frame-transformation provides a powerful approximation to the short-range reaction matrix $\mathbf{K}^{\mathrm{sr}}$ in the basis $|i\rangle$ that defines the collision channels in which the system is diagonal at large $R$ [22]:

$$K_{i,i'}^{\mathrm{sr}} = \sum_\lambda \langle i|\lambda\rangle \tan[\pi \mu_S(E)] \langle \lambda|i'\rangle. \tag{43}$$

In the absence of an external magnetic field, asymptotic channels are simply the properly symmetrized hyperfine states (7). However, if there is an applied field, the asymptotic dissociation channels are now eigenstates of the full $\mathbf{H}^{\mathrm{HZ}}$, as in Eq. (8).

The short-ranged reaction matrix obtained from Eq. (43) depends only on the single-channel quantum defects $\mu_S(E)$ and the field-dependent transformation that accomplishes the dressing. It is not entirely clear, however, at what energy $E$ one should evaluate the quantum defects when computing $K^{\mathrm{sr}}$ from Eq. (43), for the defects themselves are functions of

energy measured with respect to the common singlet and triplet thresholds (zero), while the collision energy is measured with respect to the asymptotic threshold energies $E_i^{\mathrm{th}}$ computed in Eq. (9).

As a first approximation, one may assume that the energy dependence of the quantum defects is negligible, and simply evaluate $\mu_S$ at zero energy. This results in what we call the *energy-independent frame transformation* (EIFT).

A better approximation, which results in the *energy-dependent frame transformation* (EDFT), is to evaluate $\mu_S(E)$ at the channel-weighted average energy [22]

$$\bar{E}_\lambda = \sum_i \left(E - E_i^{\mathrm{th}}\right) |\langle \lambda|i\rangle|^2. \tag{44}$$

Both of the EIFT and EDFT approximations circumvent the need to solve a set of coupled equations, allowing all scattering observables to be computed with *single* channel calculations only. The more rigorous boundary condition (21) needed for MQDT, on the other hand, requires a CC calculation in the region $R \leqslant R_m$. We refer to calculations that stem from Eq. (21) as "full" MQDT calculations, labeled as "MQDT" in the figures that follow.

## IV. RESULTS

Here, we present results for the scattering length versus magnetic field for homonuclear collisions of alkali atoms ranging from lithium to cesium. We focus on *s*-wave collisions only, and identify the positions of magnetic Feshbach resonances and zero crossings in the lowest collision channel for a given $M_F$ block. These are compiled in Table IV along with available experimental data. Empty cells in the last column indicate that we were unable to find an experimental measurement in the literature. The locations of many zeros associated with narrow resonances are difficult to observe experimentally, and several high-field resonances have yet to appear in the literature. All calculations are performed at a collision energy of 1 $\mu$K to approximate realistic experimental conditions. The scattering lengths are computed in the zero-energy limit by fitting $k \cot(\delta)$ vs $k^2$ to the low-energy effective range expansion $k \cot \delta = -\frac{1}{a} + \frac{1}{2}r_{\mathrm{eff}}k^2$ and extracting the intercept.

TABLE IV. Features in the field-dependent *s*-wave scattering length for all alkali species considered here. Calculations are performed at a collision energy of 1 $\mu$K. Results are in gauss (G).

| Atom | Feature | CC | MQDT | EDFT | EIFT | Experiment |
|---|---|---|---|---|---|---|
| $^6$Li, $M_F = 0$ | Zero | 527.407 | 527.220 | 527.200 | 526.851 | 527.5(2) [58], 528(4) [59], 530(3) [60] |
| | Pole | 543.286 | 543.284 | 543.282 | 542.934 | 543.28(1) [61], 543.286(3) [62] |
| | Zero | 543.387 | 543.384 | 543.382 | 543.034 | |
| | Pole | 832.180 | 832.186 | 831.779 | 831.527 | 834.1(1.5) [49], 822(3) [63] |
| $^7$Li, $M_F = +2$ | Zero | 140.909 | 140.917 | 139.854 | 139.614 | |
| | Zero | 543.438 | 543.435 | 544.420 | 543.573 | 543.6(1) [64] |
| | Pole | 737.716 | 737.717 | 737.949 | 736.334 | 737.69(12) [9] |
| $^{23}$Na, $M_F = +2$ | Pole | 851.074 | 851.073 | 852.215 | 865.066 | 851.0(2) [41] |
| | Zero | 851.083 | 851.083 | 852.225 | 865.076 | |
| | Pole | 905.149 | 905.147 | 905.159 | 917.777 | 905.1(4) [41] |
| | Zero | 906.193 | 906.191 | 906.203 | 918.780 | |
| $^{39}$K, $M_F = +2$ | Zero | 25.427 | 25.424 | 25.343 | 25.764 | |
| | Pole | 25.886 | 25.889 | 25.836 | 26.236 | 25.85(10) [53] |
| | Zero | 350.374 | 350.364 | 350.492 | 350.720 | 350 [65], 350.4 [53] |
| | Pole | 402.461 | 402.462 | 402.338 | 402.558 | 403.4(7) [53] |
| | Zero | 741.931 | 744.930 | 745.000 | 750.397 | |
| | Pole | 744.936 | 744.935 | 745.005 | 750.402 | |
| | Zero | 751.886 | 751.882 | 751.935 | 757.268 | |
| | Pole | 752.277 | 752.280 | 752.334 | 757.65 | 752.3(1) [53] |
| $^{40}$K, $M_F = -7$ | Pole | 12.661 | 12.661 | 13.009 | 14.557 | |
| | Zero | 12.663 | 12.663 | 13.0132 | 14.558 | |
| | Pole | 224.222 | 224.222 | 223.758 | 223.909 | 224.2(1) [66] |
| | Zero | 231.432 | 231.432 | 231.151 | 231.287 | 233.9(1) [66] |
| $^{85}$Rb, $M_F = +4$ | Zero | 850.572 | 850.571 | 847.973 | 868.110 | |
| | Pole | 851.755 | 851.755 | 850.911 | 870.204 | 852.3(3) [54] |
| | Zero | 1068.352 | 1068.352 | 1070.585 | 1087.537 | |
| | Pole | 1070.787 | 1070.787 | 1073.679 | 1092.366 | |
| $^{87}$Rb, $M_F = +2$ | Pole | 406.883 | 406.883 | 400.758 | 446.639 | 406.2(3) [67] |
| | Zero | 406.884 | 406.884 | 401.249 | 446.897 | |
| | Pole | 686.396 | 686.396 | 692.704 | 753.618 | 685.4(3) [67] |
| | Zero | 686.403 | 686.402 | 692.706 | 753.941 | |
| | Pole | 911.651 | 911.651 | 933.705 | 1008.810 | 911.7(4) [67] |
| | Zero | 911.652 | 911.652 | 933.707 | 1008.840 | |
| | Pole | 1007.71 | 1007.710 | 986.280 | 1046.440 | 1007.40(4) [68], 1007.3(4) [67] |
| | Zero | 1007.91 | 1007.910 | 986.835 | 1046.780 | 1007.60(3) [68] |
| $^{133}$Cs, $M_F = +6$ | Pole | −8.654 | −9.693 | −56.018 | 59.594 | −11.7 [56] |
| | Zero | 10.155 | 10.139 | 4.308 | 86.218 | 17.26(20) [69], 17.119(2) [70] |
| | Pole | 545.846 | 545.866 | 468.879 | 599.953 | 549 [57] |
| | Zero | 551.406 | 551.410 | 538.332 | 616.613 | 553.73(2) [57] |
| | Pole | 822.933 | 823.140 | 743.691 | 803.191 | 787 [57] |
| | Zero | 901.203 | 901.202 | 896.486 | 933.785 | |

### A. Lithium

For both isotopes of lithium, we use the MLR potentials of Refs. [39,40] but with two significant alterations. First, we use the dispersion coefficients $C_n$ tabulated in Ref. [47], which include effects arising from the finite mass of the atomic nuclei. Second, we modify the short-ranged behavior of the singlet and triplet potentials by adding a term of the form (11).

The first alteration is particularly necessary for our purpose of developing and testing the accuracy of MQDT methods because the dispersion coefficients reported in Refs. [39,40] differ for the singlet and triplet channels. It is desirable to have the *same* long-range behavior in each

collision channel for MQDT, so that the MQDT parameters $\mathcal{G}(\mathcal{E})$, $\mathcal{A}(\mathcal{E})$, $\eta(E)$, $\gamma(E)$ can be computed uniquely. Having modified the dispersion coefficients, it is essential to include the short-ranged potential in Eq. (11) in order to restore the singlet and triplet scattering lengths to physically realistic values.

References [39,40] report $^6$Li scattering lengths $a_S = 45.05(9)a_0$ and $a_T = -3602(95)a_0$, where the reported uncertainties arise from statistical errors in the direct potential fit. Our scattering length calculations using their subroutines [71] for generating the potentials "out of the box" yield $a_S/a_0 = 45.046$ and $a_T/a_0 = -3430.2$, showing excellent agreement for the singlet $a_S$, but $\approx 5\%$ discrepancy in the triplet $a_T$,
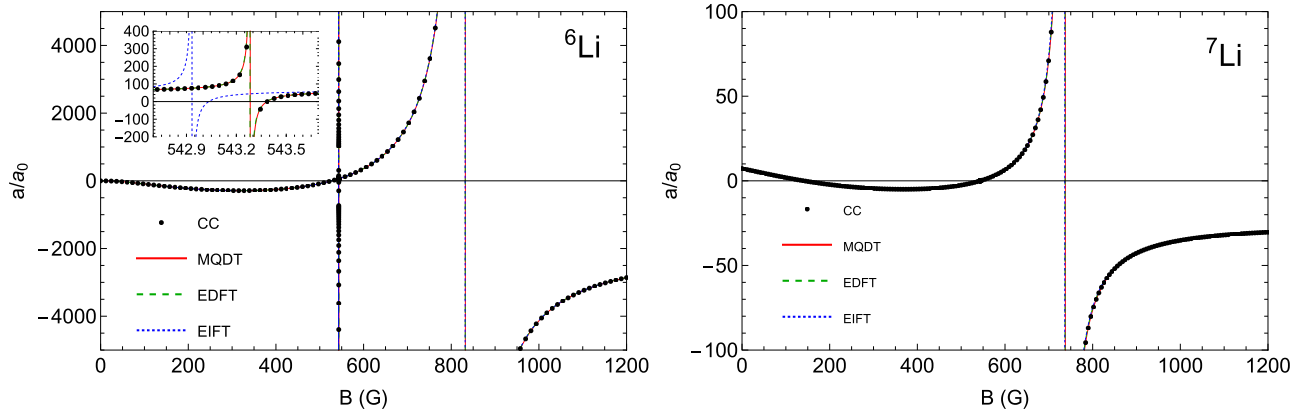
FIG. 5. The field-dependent scattering length for $^6$Li collisions with $M_F = 0$ and $^7$Li collisions in the ground state with $M_F = 2$ at collision energy 1 $\mu$K is shown. The inset on the $^6$Li plot shows the narrow resonance at 543.286 G.

for which we cannot account. We have conducted rigorous tests of our calculations, as detailed in Appendix A. The *same* code used to solve the coupled-channels problem was used to compute the singlet and triplet scattering lengths.

We adjust the parameters $V_c^{(S)}$ primarily to reproduce the scattering lengths reported in Ref. [48]. Ultimately, our reported scattering lengths for $^6$Li in Table III differ slightly from Ref. [48] because we have made additional adjustments to match the position for the narrow *s*-wave resonance near 543 G to the experimental observation of Hazlett *et al.* [62].

For $^6$Li we consider elastic collisions in the lowest channel with $M_F = 0$. Table IV lists the zeros and poles of the *s*-wave scattering length as determined by the coupled-channels (CC) calculation, MQDT, EDFT, and EIFT. The left graph in Fig. 5 plots $a(B)$ for field values ranging from zero to 1200 G. There is broad resonance near 832 G and a narrow feature around 543 G, which is shown more clearly in the inset. Both MQDT and EDFT come within 1 mG of the CC calculation for this narrow resonance, while EIFT is off by 0.3 G. However, both EDFT and EIFT slightly underestimate the location of the broad resonance at 832.18 G, whereas MQDT almost exactly agrees with the CC calculation.

Several groups have experimentally determined the resonance features of this collision [49,58–63,72]. Measurements made by Jochim *et al.* [60] and O'Hara *et al.* [59] in 2002 place the location of the first zero crossing at $530 \pm (3)$ and $528 \pm 4$ G, respectively. In 2008, Du *et al.* more accurately determined the position to be $527.5 \pm 0.2$ G [58]. Our CC calculation agrees with the latter value, while MQDT and EDFT fall just outside the experimental uncertainty. The location of the narrow resonance has been measured by Refs. [61,72]. However, to date, Hazlett *et al.* [62] has made the most precise measurement at 543.286 (3) G. We pin our model for the potential curves so that this resonance position is reproduced by our CC calculations to better than 1 mG. The results of MQDT and EDFT are nearly within the error bars of this observation. Using rf spectroscopy on weakly bound molecules, Bartenstein *et al.* [49] measured the position of the wide resonance to be 834.1(1.5) G, which our CC and MQDT calculations fall just short of.

Scattering length calculations using the potentials of Refs. [39,40] for the case of $^7$Li show reasonable but not

perfect agreement with values reported in those papers. References [39,40] find $a_S/a_0 = 34.22(9)$ and $a_T/a_0 = -27.80(2)$, while we find $a_S/a_0 = 34.222$ and $a_T/a_0 = -27.891$. As with $^6$Li, we replace the dispersion coefficients of Refs. [39,40] with those of Ref. [47]. Having done so, the parameters $V_c^{(S)}$ of Eq. (11) are adjusted to give the best agreement possible with experimental measurements of the scattering length node near 544 G and the wide resonance near 738 G. This yields scattering lengths comparable to those reported in Ref. [48].

The right plot in Fig. 5 shows the field-dependent scattering length for $^7$Li elastic collisions in the ground state with $M_F = 2$. Just as in the $^6$Li case, we find that MQDT is nearly in perfect agreement with the CC calculation, only underestimating the zero crossings in $a(B)$ by a few mG. Both EDFT and EIFT do slightly worse, coming within 1 G of the full coupled-channels calculation. Pollack *et al.* [64] observed that the scattering length passes through a zero crossing at $B_0 = 543.6(1)$ G with a slope of $\Delta a/\Delta B = 0.08 a_0$ G$^{-1}$. They fit the resonance peak to 736.8(2) G. Our best fit (performed manually) yields positions shown in Table IV. Our CC and MQDT calculations are nearly within the error bars of this observation and our calculation of the slope of $a(B)$ is $\Delta a/\Delta B = 0.079 a_0$ G$^{-1}$, in agreement with their observations.

### B. Sodium

Early experiments [73,74] reported two *s*-wave resonances for sodium atoms prepared in the $|f, m_f\rangle = |1, 1\rangle$ hyperfine state (i.e., ground state of the $M_F = +2$ block): one near 853 G and another narrower one near 907 G. The accuracy of those measurements was limited by magnetic-field stability to about 20 G. Later experiments [41] greatly improved the accuracy of these resonance positions, made additional measurements of higher partial-wave resonances, and developed improved singlet and triplet potential-energy functions of the Hannover form.

We adopt the sodium potential-energy function developed in Ref. [41] without modification. Field values for zeros and pole positions in the scattering length are tabulated in Table IV. In Fig. 6, we plot the scattering length from 820 to 930 G, showing the two *s*-wave resonances in this range. We found no other *s*-wave resonances with width greater than
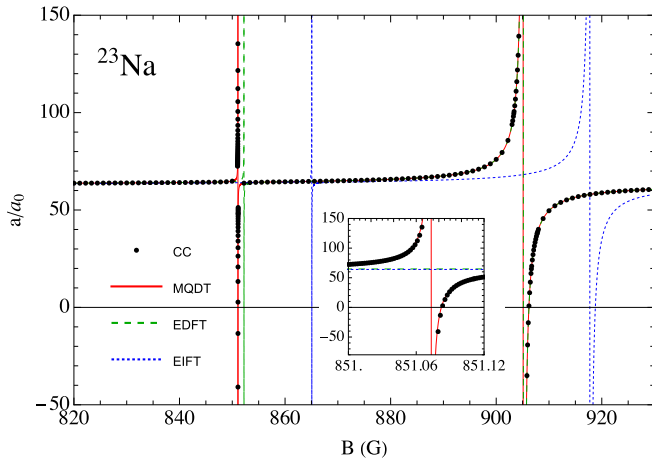
FIG. 6. The scattering length (in units of $a_0$) for $^{23}$Na collisions in the lowest channel with total $M_F = 2$ at threshold is shown as a function of magnetic field.

approximately 1 mG for fields less than 1200 G, but there is another narrow resonance at very high field (not shown) near 2055 G.

Comparing the MQDT, EDFT, and EIFT with converged CC calculations reveals that while the EIFT is able to reproduce the qualitative features of $a(B)$, the positions of resonances are consistently overestimated by about 14 G. Improvements afforded by the EDFT are significant. The position of the narrow resonance near 851 G is only overestimated by about 1 G, while the position of the wide resonance near 905 G is overestimated by only 10 mG. Moreover, our CC and MQDT calculations are in agreement with Ref. [41], which reports values of 851.0(2) and 905.1(4) G for the two resonances.

### C. Potassium

We use the potassium potential-energy functions of Ref. [42] without modification. For $^{39}$K, we consider elastic collisions in the lowest channel with $M_F = 2$. The locations of poles and zero crossings in the *s*-wave scattering length are provided in Table IV and Fig. 7(d) plots $a(B)$ for fields ranging from zero to 1200 G. Figures 7(a)–7(c) show the three narrow resonances at 25.886, 744.936, and 752.277 G in more detail. Comparing MQDT, EDFT, and EIFT with the full coupled channels calculation, we find that all three methods are able to reproduce the broad resonance near 402.461 G and the narrow resonance at 25.886 G (as determined by our CC calculations) to within 1 G. However, EIFT fares worse for the two resonances at higher fields, overestimating the locations of poles and zeros by about 5 G while both MQDT and EDFT are within 0.1 G of the CC calculation. Note that the sharp resonance in the EIFT calculation in Fig. 7(c) is the same feature shown in Fig. 7(b) for the other three calculations.

D'Errico *et al.* [53] found resonances in a number of channels. In the $M_F = 2$ block, they measured resonances at 25.85(10), 403.4(7), and 752.3(1) G, which are nearly in agreement with our CC and MQDT calculations. However, they missed a predicted narrow near 745 G. Chapurin *et al.* [75] have recently made a precise measurement of a low-field resonance in $^{39}$K in the $M_F = -2$ block, finding a resonance position 33.5820(14) G, which represents a significant improvement over an earlier measurement [8]. Our CC calculations using the unmodified potential functions of Ref. [42] yield a resonance position of 33.5780 G.

For $^{40}$K, we consider elastic collisions in the lowest channel with $M_F = -7$. The scattering length for magnetic fields between zero and 800 G is shown in Fig. 7(e). There is a very narrow resonance near 12.66 G (which is shown in greater
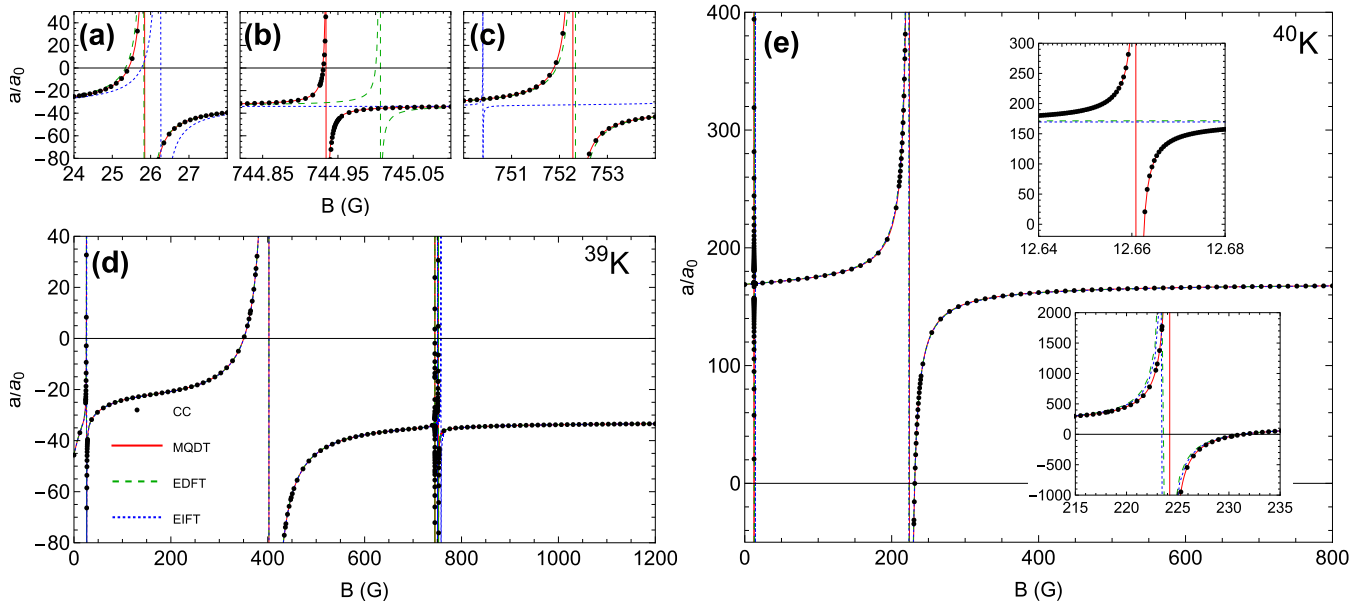


FIG. 7. (d) The scattering length (in units of $a_0$) for $^{39}$K in the lowest channel with total $M_F = 2$, with panels (a)–(c) showing the narrow resonances at 25.886, 744.936, and 752.277 G, respectively. (e) The scattering length (in units of $a_0$) for $^{40}$K collisions in the lowest channel with total $M_F = -7$ at threshold is shown as a function of magnetic field. Insets in the $^{40}$K plot show the resonances near 12 and 224 G in greater detail.
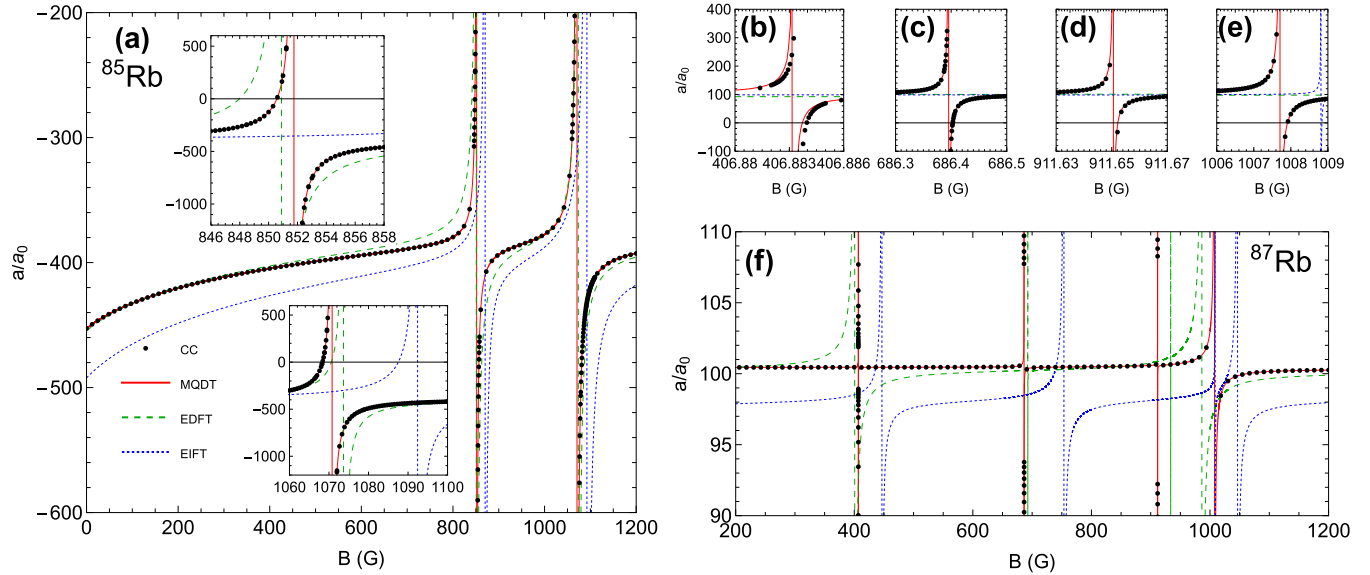
FIG. 8. (a) The scattering length (in units of $a_0$) for $^{85}$Rb collisions in the lowest channel with total $M_F = 4$ at threshold is shown as a function of magnetic field. (f) The scattering length (in units of $a_0$) for $^{87}$Rb collisions in the lowest channel with total $M_F = 2$ at threshold is shown as a function of magnetic field. (b)–(e) Zoom in on the four narrow resonance features of the $^{87}$Rb collisions near 406, 686, 911, and 1007 G, respectively.

detail in the top inset) and a broader feature near 224 G (shown in the bottom inset). Analyzing our results, we find that MQDT and CC calculations exactly agree on the location of every pole and zero crossing in $a(B)$. EDFT and EIFT are slightly less accurate, differing from the coupled-channels calculation by $\approx 1$ G. Looking at available experimental data, Ref. [66] determined the position of the broad resonance to be $224.21 \pm 0.05$ G, with a width $\Delta = 9.7 \pm 0.6$ G, which nearly agrees with our CC calculation.

### D. Rubidium

We use the potential-energy functions for rubidium developed by Strauss *et al.* [43] without modification. For both isotopes there are small, yet significant differences between the scattering lengths reported in Ref. [43] and those that we calculate using the same potential model. We have not been able to determine the source of this discrepancy, but the disagreement motivated us to perform further rigorous tests of our log-derivative propagator. The results of these tests are carried out in Appendix A.

For $^{85}$Rb, we consider elastic collisions in the lowest channel with total $M_F = 4$. Field values for the zeros and poles in the scattering length are given in Table IV. Our results for MQDT, EIFT, and EDFT compared with the full coupled channels calculation (CC) are shown in Fig. 8(a) where we plot the scattering length for fields ranging from zero to 1200 G. Coupled channels calculations reveal two broad resonances at 851.755 G and 1070.9 G which are shown more clearly in the insets. We find that all methods are able to replicate the general properties of the scattering length, but MQDT

is superior for predicting the positions of resonances and zero crossings, matching the CC results almost exactly. EDFT does slightly worse, coming within a few gauss of the CC results, while EIFT is the least accurate, routinely overestimating the locations of poles and zeroes by about 20 G. In 2013, Blackley *et al.* [54] experimentally confirmed 17 Feshbach resonances in optically trapped $^{85}$Rb. For the ground-state channel, they report one *s*-wave Feshbach resonance at 852.3(3) G with a width $\Delta > 1$ G. Our CC and MQDT calculations fall just outside the uncertainty of this measurement. To the best of our knowledge, no experimental measurements of the high-field resonance near 1071 G has appeared in the literature.

For $^{87}$Rb, we consider elastic collisions in the lowest channel with total $M_F = 2$. Figure 8(f) plots the scattering length for fields between 200 and 1200 G and Figs. 8(b)–8(e) zoom in on each of the four resonance features. Similar to the $^{85}$Rb case, we find that MQDT almost exactly reproduces the results of coupled channels calculation while EIFT overestimates the positions of poles and EDFT comes within 10 G of the CC results. Turning to experimental data, in 2002, Marte *et al.* [67] observed more than 40 resonances in rubidium 87 for magnetic fields between 0.5 and 1260 G for various spin mixtures in the lower hyperfine ground state to an accuracy of 30 mG. For the ground-state entrance channel, they report *s*-wave Feshbach resonances at 406.2(3), 685.4(3), 911.7(4), and 1007.3(4) G. A more recent study conducted by Ref. [68] places the high-field resonance at 1007.40(4) G and measures a zero crossing in the scattering length at 1007.60(3) G. We find that the values predicted by our CC and MQDT calculations are nearly within the experimental uncertainty of both Refs. [67,68].

### E. Cesium

For cesium, we use the MLR potentials of Ref. [44], but with modifications as discussed in Sec. II B. We modify the long-range behavior of the potential to more rapidly converge to the functional form of $V_{LR}(R)$ in Eq. (5) by using a switching function $f(R)$ that vanishes for $R \lesssim R_{LR} - \delta R$ and goes to unity for $R \gtrsim R_{LR} + \delta R$,

$$V^{(S)}(R) = V_S^{(MLR)}(R)[1 - f(R)] + f(R)V_{LR}(R), \quad (45)$$

where the switching function is

$$f(R) = \frac{1}{2}\left[\tanh\left(\frac{R - R_{LR}}{\delta R}\right) + 1\right]. \quad (46)$$

We choose $\delta R = 0.5a_0$ and $R_{LR} = 38a_0$ to ensure that when the boundary condition Eq. (21) determining $\mathbf{K}_{sr}$ is applied in at $R_f = 40a_0$, the reference functions $\hat{f}(R)$ and $\hat{g}(R)$ are valid solutions to the Schrödinger equation in each channel. Without the switching function, there is little hope of finding agreement between the CC and MQDT calculations for this particular MLR potential. Choosing a smaller $R_{LR}$ gives better agreement between the CC and MQDT calculations but also dramatically changes the values of $a_S$, $a_T$, the background scattering length, and the resonance positions—so much so that tuning the parameters $V_c^{(S)}$ in order to bring $a_S$ and $a_T$ back in line with accepted values becomes difficult. If better agreement with CC calculations is desired, either a more detailed reparametrization of the potential model is required or a different model should be used.

The switching function turns out to be unnecessary for the case of lithium, despite the fact that the lithium MLR potentials exhibit similar slow convergence to the form of $V_{LR}$ (see Fig. 3). We speculate that this is likely because the lower reduced mass of the lithium dimer leads to a correspondingly slower phase accumulation in the asymptotic region.

As with lithium, we adjust the short-range behavior of the MLR potentials by adding a quadratic term given by (11). We first adjust the parameters $V_c^{(S)}$ to reproduce the scattering lengths reported in Ref. [56] then make further adjustments to best reproduce the positions of the three *s*-wave resonances reported in Ref. [57]. It is not possible to reproduce all three resonance positions by tuning only $V_c^{(S)}$, and a full reparametrization of the potential is beyond the scope of this work.

Field values for zeros and pole positions in the scattering length are listed in Table IV. In Fig. 9, we plot the scattering length, showing three *s*-wave resonances for a magnetic field ranging from $-50$ to 1100 G. Comparing MQDT, EDFT, and EIFT to the converged CC calculations shows that, while all three methods are able to reproduce the qualitative features of $a(B)$, MQDT by far is the most successful at replicating the locations of resonances and zero crossings, agreeing to within 1 G. Conversely, EIFT overshoots the resonances near $-10$ and 545 G by about 50 G, and underestimates the resonance near 820 G by 20 G. EDFT does even worse, undershooting the three resonances by about 80 G. However, EDFT does slightly better at predicting the locations of zero crossing, matching the CC calculations to within 10 G.

The low-field (i.e., $B \lesssim 250$ G) resonances of cesium atoms have been studied by several groups [56,69,70,76–81].
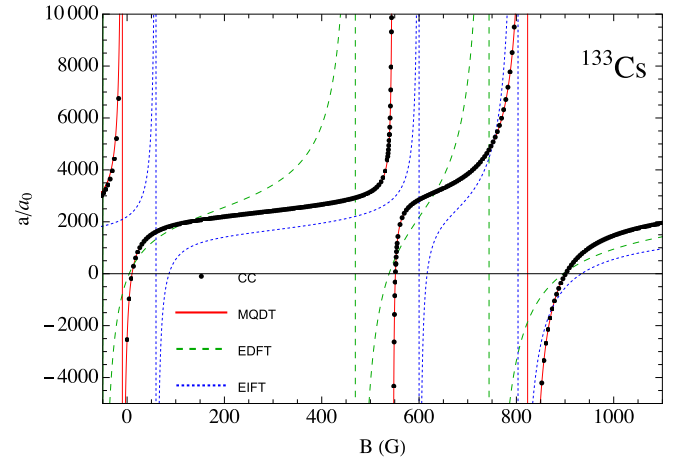


FIG. 9. The scattering length (in units of $a_0$) for $^{133}$Cs collisions in the lowest channel with total $M_F = 6$ at threshold is shown as a function of magnetic field.

In 1999, Vuletic *et al.* [76] observed a low-field resonance in the total $M_F = 6$ block. They found a zero and a pole at the following positions: 17.0(2) and 30(3) G. Subsequently, Refs. [70,77] reported values of $(17.064 \pm 0.056)$ and 17.119(2) G, respectively, for the position of the zero crossing in the scattering length. More recently, Ref. [69] find the zero crossing to be at 17.26(20) G. Our CC and MQDT calculations differ from this latest experimental value by $\approx 7$ G. The discrepancy may be improved by employing interaction potentials such as the M2012 model of Ref. [57].

The zero at 17 G has been used [70,81] to prepare a Bose-Einstein condensate (BEC) of cesium atoms in the ground state. This feature is associated with a broad Feshbach resonance near $-11$ G. Physically, a resonance at $-|B|$ corresponds to one at $|B|$ with the spin projections of each atom reversed in sign [1]. In this case, the negative resonance at $-11.7$ G in the $M_F = +6$ block corresponds to a positive resonance at 11.7 G in the $M_F = -6$ block, which as been measured by Ref. [56]. Other theoretical models predict a location of $-11.1(6)$ G [82] or $-12$ G [57] for this low-field *s*-wave resonance. Comparing our results to these values, we find that both the coupled-channels calculation and MQDT overestimate this resonance position by $\approx 3$ G.

Berninger *et al.* [57] have explored the high-field physics of ultracold cesium collisions. Using trap-loss spectroscopy, they observed two broad loss features around 549 and 787 G, which correspond to *s*-wave resonances, and a zero crossing in the scattering length at 553.73(2) G. Again, we see a discrepancy between the available experimental data and our calculations. The coupled-channels calculation and MQDT underestimate the first resonance position and the zero crossing by a few gauss, and overestimate the latter resonance position by almost 50 G. This is a shortcoming of the MLR potential developed in Ref. [44] for cesium, and we expect significantly better agreement in future calculations using improved potential models such as the M2012 potential of Ref. [57], which was specifically developed to describe experimental data at *both* low and high fields.
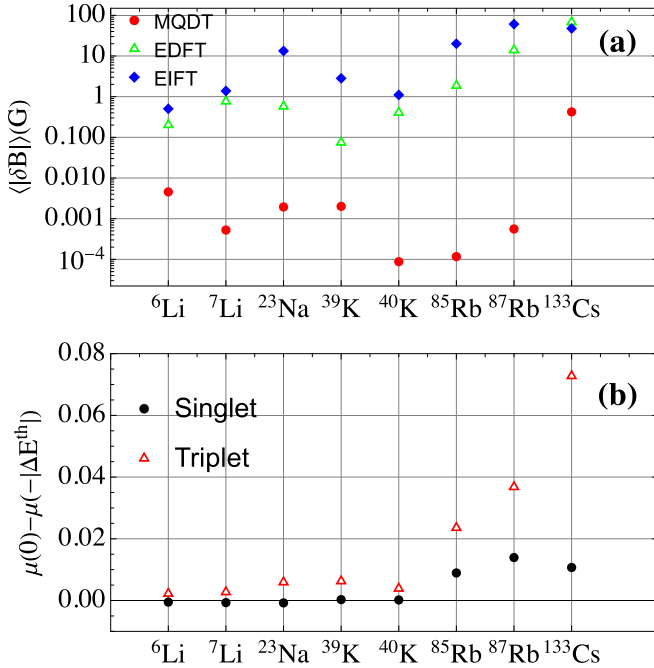
FIG. 10. Panel (a) shows the average absolute error (in gauss) of resonance positions for each atomic species. Data for MQDT (red circles), EDFT (green triangles), and EIFT (blue diamonds) are all shown on a log scale. Panel (b) shows the variation of the singlet and triplet quantum defects over the necessary range of energy required for the energy-dependent frame transformation calculation.

## V. CONCLUDING DISCUSSION

The accuracy of the EIFT, EDFT, and MQDT calculations depend on a number of factors that we will now attempt to untangle. In Fig. 10(a), we show the mean absolute error (in gauss) of magnetic Feshbach resonance positions for each atomic species. The error is defined for each of the resonance (pole) positions in Table IV simply as

$$\delta B = \left| B_{\text{pole}}^{\text{type}} - B_{\text{pole}}^{\text{CC}} \right|, \tag{47}$$

where "type" stands for any of the MQDT, EDFT, or EIFT calculations, and CC stands for the coupled channels calculation, which we have ensured are fully converged. We have taken care to compute a higher density of points in the vicinity of resonance poles and zeros of the scattering length. An interpolating function is used to identify the zeros of $1/a(B)$ as pole locations, accelerating the convergence of the CC calculations in particular when searching for these features.

Let us first consider the elements of the MQDT calculation that may limit its accuracy. First, and likely the most significant contributor to error, is the fact that the MLR potentials themselves converge rather slowly to their asymptotic form, as illustrated in Fig. 3. Therefore, the reference functions $\hat{f}(R)$ and $\hat{g}(R)$, which are solutions to the Schrödinger equation in a potential $V_{\text{LR}}$, are not perfect solutions to the Schrödinger equation in $V^{\text{MLR}}$. Even slight differences in the long-range potentials can lead to a substantial difference in the resonance position. Second, the reference functions themselves are computed numerically and any error in their computation is inherited by $\mathbf{K}_{\text{sr}}$. The MQDT calculations (red circles)

are typically several orders of magnitude more accurate than either of the frame transformation calculations, but MQDT performs most poorly for $^6$Li and $^{133}$Cs. We believe that this is primarily caused by the slow convergence of the MLR potentials to the asymptotic form $V_{\text{LR}}$ of Eq. (5), as shown in Fig. 3. Without the switching function Eq. (46), the MQDT calculation for $^{133}$Cs is significantly poorer. Likewise, without extending the matching radius $R_m$ out to about $55a_0$ for lithium, as discussed in Sec. II B, the performance of MQDT is significantly worse than what is shown. For further improvements, we recommend using a different potential-energy model with faster convergence to $V_{\text{LR}}$.

The frame transformation calculations rely upon the singlet and triplet quantum defects $\mu_S$ which are plotted in Fig. 4. Fig. 10(b) shows the overall variation of the quantum defects over the total energy range required for the EDFT calculation, as prescribed by Eq. (44). The first feature to note is that, as a rule, the energy dependence of the triplet quantum defects is greater than that of the singlet defects. This is sensible since the separation of energy and length scales is more robust for the comparatively deep singlet channel, leading to weaker energy dependence in $\mu_0(E)$ compared with $\mu_1(E)$. The second feature to note is that the performance of the frame transformation calculations is strongly correlated to the energy dependence of the quantum defects themselves. In general, the heavier the species, the greater the sensitivity to energy displayed by the quantum defects. This is because the hyperfine-Zeeman splitting increases with atomic mass. The one exception to this trend is $^{40}$K, in which there are only three collision thresholds with total $M_F = -7$, and the range of energies over which one must evaluate the quantum defects is considerably smaller.

Only the MQDT calculation is able to reliably reproduce the position of every resonance pole to less than the width of the resonance. See, for example, Figs. 8(a)–8(d) showing the individual s-wave resonances in $^{87}$Rb. The discrepancies in resonance positions greater than $\approx 1$ mG are not believed to arise from the numerical precision of the ODE integration techniques (i.e., the log-derivative propagator or Runge-Kutta methods for the MQDT functions, etc.), but rather from lingering differences between the exact potential-energy functions and the reference potentials. We have conducted convergence tests to ensure that the results are converged with respect to step size, similar to those shown in Appendix A.

The EDFT provides a significant improvement over EIFT in all cases, except for cesium. For example, see the wide resonance in $^{23}$Na near 915 G shown in Fig. 6, the resonances near 26 and 752 G in $^{39}$K shown in Fig. 7, or even the two resonances shown in the insets of Fig. 8(a) for $^{85}$Rb.

To conclude, we have conducted a comprehensive study of ultracold homonuclear collisions for eight alkali species, applying three variations of multichannel quantum-defect theory that differ in how they characterize the short-ranged $K$ matrix, $\mathbf{K}_{\text{sr}}$. We have attempted to untangle various sources of error, both among the calculations themselves, and with experiment. We have quantitatively demonstrated how the frame transformation calculations become rather unreliable for the heavier species with large hyperfine-Zeeman splittings, while MQDT remains robust provided that the singlet and triplet potentials converge sufficiently quickly to the long-range form of $V_{\text{LR}}$.
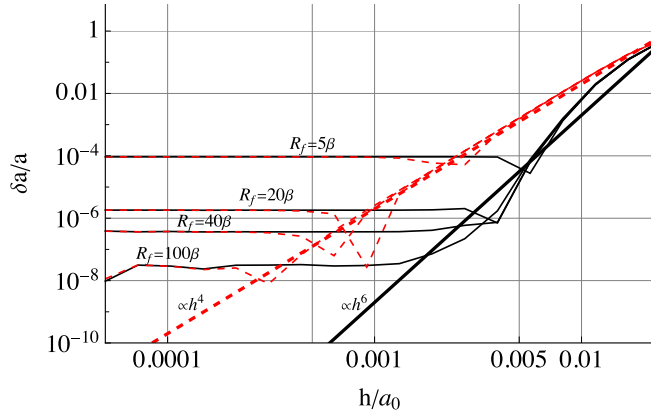
FIG. 11. Convergence tests for the scattering length using the two-channel model of Ref. [83] are shown.

We hope to perform calculations in the future that extend this work to higher partial waves and include the weak magnetic dipole-dipole coupling. A still more comprehensive study of inelastic processes is also within reach.

### ACKNOWLEDGMENTS

### APPENDIX A: NUMERICAL TESTING OF THE LOG-DERIVATIVE PROPAGATOR

Numerical discrepancies between (some of) our calculated singlet and triplet scattering lengths and those reported in the literature, particularly for rubidium, spurred us to conduct further testing of our computer code. Here, we present calculations using the two-channel test model of Ref. [83].

The authors of Ref. [83] compare three robust methods commonly used for solving coupled channels problems: (1) the integral equation method (IEM) [84], (2) the finite element [85,86] eigenchannel *R*-matrix [87] propagator, and (3) the Gordon algorithm [88]. Of these three methods, the greatest stability is achieved by the IEM, which—when used with a perturbative long-range correction—gives the scattering length to 11 significant figures $a(\infty) = 851.981\,715\,74$. We directly compare our calculation of the scattering length, $a$, to $a(\infty)$, and plot $(\delta a)/a = [a - a(\infty)]/a(\infty)$ as a function of step size $h/a_0$. Our implementation of Johnson's log-derivative propagator [26] uses Richardson extrapolation with step doubling [89], which greatly improves the convergence scaling with step size from $h^4$ to $h^6$. We therefore present two sets of calculations in Fig. 11. One with Richardson extrapolation (solid black curves), and one without (red dashed curves). The thick red dashed line indicates $h^4$ scaling, while the thick

black solid line indicates $h^6$ scaling. Calculations for various values of $R_f$ (where the matching to Bessel functions is made) are shown. These results clearly demonstrate the improved scaling, the dependence on $R_f$, and the dependence on step size $h/a_0$. We typically use $N = 10^7$ integration steps and integrate out to $R_f = 20\beta \lesssim 4000a_0$ in all our log-derivative calculations. Calculations including higher partial waves will require a larger matching radius. Based on the results shown in Fig. 11, we expect about six significant figures in the scattering length.

### APPENDIX B: NUMERICAL SOLUTION FOR THE REFERENCE FUNCTIONS $\hat{f}$ AND $\hat{g}$

The reference functions $\hat{f}_i(R)$ and $\hat{g}_i(R)$ [see Eq. (14)] are obtained from the Milne equation (15), with WKB-like boundary conditions (16) imposed at $R_x \approx 0.07\beta$, deep in the long-range reference potential $V_{LR}(R)$. To evaluate the positive-energy parameters given in Eqs. (29), (30), and (25) we compute the reference functions out to $R_F \approx 20\beta$. Meanwhile, the parameter $\cot(\gamma)$ must be evaluated via Eq. (32) at negative energies comparable to the separations of two-atom hyperfine-Zeeman splittings at magnetic-field strengths of order 1000 G. It is therefore convenient to be able to compute solutions to Eq. (15) at *both* positive and negative energies out to $R = R_F$. For negative energies, however, $R_F$ lies well into the classically forbidden region where the solution $\alpha(R)$ grows without bound. To ensure numerical stability, we perform a simple variable transformation of the Milne equation by letting $\alpha(R) = e^{x(R)}$, leading to the following nonlinear equation for $x(R)$:

$$x'' + (x')^2 = e^{-4x} - k^2. \tag{B1}$$

We solve Eq. (B1) by fourth order Runge-Kutta (RK4) with repeated step doubling and Richardson extrapolation (repeated twice) [90]. To be clear, we define $y_1(R) = x$, and $y_2(R) = x'(R)$. Then apply the usual RK4 [89] procedure to the set of coupled equations:

$$\begin{pmatrix} y_1' \\ y_2' \end{pmatrix} = \begin{pmatrix} y_2 \\ e^{-4y_1} - k^2 - y_2^2 \end{pmatrix}. \tag{B2}$$

The log-derivatives of the reference functions are easily computed:

$$\frac{\hat{f}'}{\hat{f}} = y_2 + e^{-2y_1} \cot[\phi(R) + \phi_L], \tag{B3}$$

$$\frac{\hat{g}'}{\hat{g}} = y_2 - e^{-2y_1} \tan[\phi(R) + \phi_L], \tag{B4}$$

where $\alpha(R) = e^{y_1(R)}$. This provides a numerically stable way to compute all necessary quantities, including the phase standardization from Eq. (20).

[1] C. Chin, R. Grimm, P. Julienne, and E. Tiesinga, Feshbach resonances in ultracold gases, Rev. Mod. Phys. **82**, 1225 (2010).

[2] I. Bloch, J. Dalibard, and W. Zwerger, Many-body physics with ultracold gases, Rev. Mod. Phys. **80**, 885 (2008).

[3] C. A. Regal, C. Ticknor, J. L. Bohn, and D. S. Jin, Creation of ultracold molecules from a Fermi gas of atoms, Nature (London) **424**, 47 (2003).

[4] M. Berninger, A. Zenesini, B. Huang, W. Harm, H.-C. Nägerl, F. Ferlaino, R. Grimm, P. S. Julienne, and J. M. Hutson,

Universality of the three-body parameter for Efimov states in ultracold cesium, Phys. Rev. Lett. **107**, 120401 (2011).

[5] T. Kraemer, M. Mark, P. Waldburger, J. G. Danzl, C. Chin, B. Engeser, A. D. Lange, K. Pilch, A. Jaakkola, H.-C. Nägerl *et al.*, Evidence for Efimov quantum states in an ultracold gas of caesium atoms, Nature (London) **440**, 315 (2006).

[6] F. Ferlaino, S. Knoop, M. Berninger, W. Harm, J. P. D'incao, H.-C. Nägerl, and R. Grimm, Evidence for universal four-body states tied to an Efimov trimer, Phys. Rev. Lett. **102**, 140401 (2009).

[7] B. Huang, L. A. Sidorenkov, R. Grimm, J. M. Hutson *et al.*, Observation of the second triatomic resonance in Efimov's scenario, Phys. Rev. Lett. **112**, 190401 (2014).

[8] S. Roy, M. Landini, A. Trenkwalder, G. Semeghini, G. Spagnolli, A. Simoni, M. Fattori, M. Inguscio, and G. Modugno, Test of the universality of the three-body Efimov parameter at narrow Feshbach resonances, Phys. Rev. Lett. **111**, 053202 (2013).

[9] P. Dyke, S. E. Pollack, and R. G. Hulet, Finite-range corrections near a Feshbach resonance and their role in the Efimov effect, Phys. Rev. A **88**, 023625 (2013).

[10] M. Seaton, The quantum defect method, Mon. Not. R. Astron. Soc. **118**, 504 (1958).

[11] M. Seaton, Quantum defect theory I. general formulation, Proc. Phys. Soc., London **88**, 801 (1966).

[12] M. Seaton, Quantum defect theory II. Illustrative one-channel and two-channel problems, Proc. Phys. Soc., London **88**, 815 (1966).

[13] C. H. Greene, U. Fano, and G. Strinati, General form of the quantum-defect theory, Phys. Rev. A **19**, 1485 (1979).

[14] C. H. Greene, A. R. P. Rau, and U. Fano, General form of the quantum-defect theory. II, Phys. Rev. A **26**, 2441 (1982).

[15] F. H. Mies, A multichannel quantum defect analysis of diatomic predissociation and inelastic atomic scattering, J. Chem. Phys. **80**, 2514 (1984).

[16] F. H. Mies and P. S. Julienne, A multichannel quantum defect analysis of two-state couplings in diatomic molecules, J. Chem. Phys. **80**, 2526 (1984).

[17] B. Gao, Solutions of the Schrödinger equation for an attractive $1/r^6$ potential, Phys. Rev. A **58**, 1728 (1998).

[18] B. Gao, Quantum-defect theory of atomic collisions and molecular vibration spectra, Phys. Rev. A **58**, 4222 (1998).

[19] B. Gao, Zero-energy bound or quasibound states and their implications for diatomic systems with an asymptotic van der Waals interaction, Phys. Rev. A **62**, 050702(R) (2000).

[20] B. Gao, Angular-momentum-insensitive quantum-defect theory for diatomic systems, Phys. Rev. A **64**, 010701(R) (2001).

[21] B. Gao, E. Tiesinga, C. J. Williams, and P. S. Julienne, Multichannel quantum-defect theory for slow atomic collisions, Phys. Rev. A **72**, 042719 (2005).

[22] J. P. Burke, Jr., C. H. Greene, and J. L. Bohn, Multichannel cold collisions: Simple dependences on energy and magnetic field, Phys. Rev. Lett. **81**, 3355 (1998).

[23] T. M. Hanna, E. Tiesinga, and P. S. Julienne, Prediction of Feshbach resonances from three input parameters, Phys. Rev. A **79**, 040701(R) (2009).

[24] B. Gao, Analytic description of atomic interaction at ultracold temperatures. II. Scattering around a magnetic Feshbach resonance, Phys. Rev. A **84**, 022706 (2011).

[25] Y. Cui, M. Deng, L. You, B. Gao, and M. K. Tey, Broad Feshbach resonances in ultracold alkali-metal systems, Phys. Rev. A **98**, 042708 (2018).

[26] B. Johnson, The multichannel log-derivative method for scattering calculations, J. Comput. Phys. **13**, 445 (1973).

[27] B. Yoo and C. H. Greene, Implementation of the quantum-defect theory for arbitrary long-range potentials, Phys. Rev. A **34**, 1635 (1986).

[28] W. Milne, The numerical determination of characteristic numbers, Phys. Rev. **35**, 863 (1930).

[29] B. P. Ruzic, C. H. Greene, and J. L. Bohn, Quantum defect theory for high-partial-wave cold collisions, Phys. Rev. A **87**, 032706 (2013).

[30] W. I. McAlexander, Ph.D. thesis, Rice University, 2000 (unpublished).

[31] H. T. C. Stoof, J. M. V. A. Koelman, and B. J. Verhaar, Spin-exchange and dipole relaxation rates in atomic hydrogen: Rigorous and simplified calculations, Phys. Rev. B **38**, 4688 (1988).

[32] E. Arimondo, M. Inguscio, and P. Violino, Experimental determinations of the hyperfine structure in the alkali atoms, Rev. Mod. Phys. **49**, 31 (1977).

[33] G. Breit and I. Rabi, Measurement of nuclear spin, Phys. Rev. **38**, 2082 (1931).

[34] C. Makrides and B. Gao, Multichannel quantum-defect theory for magnetic Feshbach resonances in heteronuclear group-I systems, Phys. Rev. A **89**, 062718 (2014).

[35] H. Knöckel, B. Bodermann, and E. Tiemann, High precision description of the rovibronic structure of the $I_2$ B-X spectrum, Eur. Phys. J. D **28**, 199 (2004).

[36] E. J. Salumbides, K. S. Eikema, W. Ubachs, U. Hollenstein, H. Knöckel, and E. Tiemann, Improved potentials and Born-Oppenheimer corrections by new measurements of transitions of $^{129}I_2$ and $^{127}I\,^{129}I$ in the $B\,^3\Pi_{0_u^+}$ -$X\,^1\Sigma_g^+$ band system, Eur. Phys. J. D **47**, 171 (2008).

[37] R. J. Le Roy, Y. Huang, and C. Jary, An accurate analytic potential function for ground-state $N_2$ from a direct-potential-fit analysis of spectroscopic data, J. Chem. Phys. **125**, 164310 (2006).

[38] R. J. L. Roy and R. D. Henderson, A new potential function form incorporating extended long-range behaviour: Application to ground-state $Ca_2$, Mol. Phys. **105**, 663 (2007).

[39] R. J. Le Roy, N. S. Dattani, J. A. Coxon, A. J. Ross, P. Crozet, and C. Linton, Accurate analytic potentials for $Li_2(X\,^1\Sigma_g^+)$ and $Li_2(A\,^1\Sigma_u^+)$ from 2 to 90 Å, and the radiative lifetime of Li(2p), J. Chem. Phys. **131**, 204309 (2009).

[40] N. S. Dattani and R. J. Le Roy, A DPF data analysis yields accurate analytic potentials for $Li_2(a\,^3\Sigma_u^+)$ and $Li_2(1\,^3\Sigma_g^+)$ that incorporate 3-state mixing near the $1\,^3\Sigma_g^+$ state asymptote, J. Mol. Spectrosc. **268**, 199 (2011).

[41] S. Knoop, T. Schuster, R. Scelle, A. Trautmann, J. Appmeier, M. K. Oberthaler, E. Tiesinga, and E. Tiemann, Feshbach spectroscopy and analysis of the interaction potentials of ultracold sodium, Phys. Rev. A **83**, 042704 (2011).

[42] S. Falke, H. Knöckel, J. Friebe, M. Riedmann, E. Tiemann, and C. Lisdat, Potassium ground-state scattering parameters and Born-Oppenheimer potentials from molecular spectroscopy, Phys. Rev. A **78**, 012503 (2008).

[43] C. Strauss, T. Takekoshi, F. Lang, K. Winkler, R. Grimm, J. Hecker Denschlag, and E. Tiemann, Hyperfine, rotational, and vibrational structure of the $a^3\Sigma_u^+$ state of $^{87}$Rb$_2$, Phys. Rev. A **82**, 052514 (2010).

[44] J. Baldwin, Master's thesis, University of Waterloo, 2012 (unpublished).

[45] J. A. Coxon and P. G. Hajigeorgiou, The ground $X^1\Sigma_g^+$ electronic state of the cesium dimer: Application of a direct potential fitting procedure, J. Chem. Phys. **132**, 094105 (2010).

[46] V. B. Sovkov, F. Xie, A. M. Lyyra, E. H. Ahmed, J. Ma, and S. Jia, Re-examination of the Cs$_2$ ground singlet $X^1\Sigma_g^+$ and triplet $a^3\Sigma_u^+$ states, J. Chem. Phys. **147**, 104301 (2017).

[47] L.-Y. Tang, Z.-C. Yan, T.-Y. Shi, and J. F. Babb, Nonrelativistic *ab initio* calculations for $2^2S$, $2^2P$, and $3^2D$ lithium isotopes: Applications to polarizabilities and dispersion interactions, Phys. Rev. A **79**, 062712 (2009).

[48] P. S. Julienne and J. M. Hutson, Contrasting the wide Feshbach resonances in $^6$Li and $^7$Li, Phys. Rev. A **89**, 052715 (2014).

[49] M. Bartenstein, A. Altmeyer, S. Riedl, R. Geursen, S. Jochim, C. Chin, J. H. Denschlag, R. Grimm, A. Simoni, E. Tiesinga *et al.*, Precise determination of $^6$Li cold collision parameters by radio-frequency spectroscopy on weakly bound molecules, Phys. Rev. Lett. **94**, 103201 (2005).

[50] E. R. I. Abraham, W. I. McAlexander, J. M. Gerton, R. G. Hulet, R. Côté, and A. Dalgarno, Triplet s-wave resonance in $^6$Li collisions and scattering lengths of $^6$Li and $^7$Li, Phys. Rev. A **55**, R3299 (1997).

[51] C. Samuelis, E. Tiesinga, T. Laue, M. Elbs, H. Knöckel, and E. Tiemann, Cold atomic collisions studied by molecular spectroscopy, Phys. Rev. A **63**, 012710 (2000).

[52] F. A. van Abeelen and B. J. Verhaar, Determination of collisional properties of cold Na atoms from analysis of bound-state photoassociation and Feshbach resonance field data, Phys. Rev. A **59**, 578 (1999).

[53] C. D'Errico, M. Zaccanti, M. Fattori, G. Roati, M. Inguscio, G. Modugno, and A. Simoni, Feshbach resonances in ultracold $^{39}$K, New J. Phys. **9**, 223 (2007).

[54] C. L. Blackley, C. R. Le Sueur, J. M. Hutson, D. J. McCarron, M. P. Koppinger, H.-W. Cho, D. L. Jenkin, and S. L. Cornish, Feshbach resonances in ultracold rubidium 85, Phys. Rev. A **87**, 033611 (2013).

[55] J. L. Roberts, N. R. Claussen, J. P. Burke, Jr., C. H. Greene, E. A. Cornell, and C. Wieman, Resonant magnetic field control of elastic scattering in cold $^{85}$Rb, Phys. Rev. Lett. **81**, 5109 (1998).

[56] C. Chin, V. Vuletić, A. J. Kerman, S. Chu, E. Tiesinga, P. J. Leo, and C. J. Williams, Precision Feshbach spectroscopy of ultracold Cs$_2$, Phys. Rev. A **70**, 032701 (2004).

[57] M. Berninger, A. Zenesini, B. Huang, W. Harm, H.-C. Nägerl, F. Ferlaino, R. Grimm, P. S. Julienne, and J. M. Hutson, Feshbach resonances, weakly bound molecular states, and coupled-channel potentials for cesium at high magnetic fields, Phys. Rev. A **87**, 032517 (2013).

[58] X. Du, L. Luo, B. Clancy, and J. E. Thomas, Observation of anomalous spin segregation in a trapped Fermi gas, Phys. Rev. Lett. **101**, 150401 (2008).

[59] K. M. O'Hara, S. L. Hemmer, S. R. Granade, M. E. Gehm, J. E. Thomas, V. Venturi, E. Tiesinga, and C. J. Williams, Measurement of the zero crossing in a Feshbach resonance of fermionic $^6$Li, Phys. Rev. A **66**, 041401(R) (2002).

[60] S. Jochim, M. Bartenstein, G. Hendl, J. H. Denschlag, R. Grimm, A. Mosk, and M. Weidemüller, Magnetic field control of elastic scattering in a cold gas of fermionic lithium atoms, Phys. Rev. Lett. **89**, 273202 (2002).

[61] C. H. Schunck, M. W. Zwierlein, C. A. Stan, S. M. F. Raupach, W. Ketterle, A. Simoni, E. Tiesinga, C. J. Williams, and P. S. Julienne, Feshbach resonances in fermionic $^6$Li, Phys. Rev. A **71**, 045601 (2005).

[62] E. L. Hazlett, Y. Zhang, R. W. Stites, and K. M. O'Hara, Realization of a resonant Fermi gas with a large effective range, Phys. Rev. Lett. **108**, 045304 (2012).

[63] M. W. Zwierlein, C. A. Stan, C. H. Schunck, S. M. F. Raupach, A. J. Kerman, and W. Ketterle, Condensation of pairs of fermionic atoms near a Feshbach resonance, Phys. Rev. Lett. **92**, 120403 (2004).

[64] S. E. Pollack, D. Dries, M. Junker, Y. P. Chen, T. A. Corcovilos, and R. G. Hulet, Extreme tunability of interactions in a $^7$Li Bose-Einstein condensate, Phys. Rev. Lett. **102**, 090402 (2009).

[65] M. Fattori, C. D'Errico, G. Roati, M. Zaccanti, M. Jona-Lasinio, M. Modugno, M. Inguscio, and G. Modugno, Atom interferometry with a weakly interacting Bose-Einstein condensate, Phys. Rev. Lett. **100**, 080405 (2008).

[66] C. A. Regal and D. S. Jin, Measurement of positive and negative scattering lengths in a Fermi gas of atoms, Phys. Rev. Lett. **90**, 230404 (2003).

[67] A. Marte, T. Volz, J. Schuster, S. Durr, G. Rempe, E. G. M. van Kempen, and B. J. Verhaar, Feshbach resonances in rubidium 87: precision measurement and analysis, Phys. Rev. Lett. **89**, 283202 (2002).

[68] T. Volz, S. Durr, S. Ernst, A. Marte, and G. Rempe, Characterization of elastic scattering near a Feshbach resonance in $^{87}$Rb, Phys. Rev. A **68**, 010702(R) (2003).

[69] T. Mežnaršič, T. Arh, J. Brence, J. Pišljar, K. Gosar, Ž. Gosar, E. Zupanič, P. Jeglič *et al.*, Cesium bright matter-wave solitons and soliton trains, Phys. Rev. A **99**, 033625 (2019).

[70] M. Gustavsson, E. Haller, M. J. Mark, J. G. Danzl, G. Rojas-Kopeinig, and H.-C. Nagerl, Control of interaction-induced dephasing of Bloch oscillations, Phys. Rev. Lett. **100**, 080404 (2008).

[71] A request for the codes may be made at http://scienide2.uwaterloo.ca/~rleroy/potentials/Li2-XAac/.

[72] K. E. Strecker, G. B. Partridge, and R. G. Hulet, Conversion of an atomic Fermi gas to a long-lived molecular Bose gas, Phys. Rev. Lett. **91**, 080406 (2003).

[73] S. Inouye, M. Andrews, J. Stenger, H.-J. Miesner, D. M. Stamper-Kurn, and W. Ketterle, Observation of Feshbach resonances in a Bose–Einstein condensate, Nature (London) **392**, 151 (1998).

[74] J. Stenger, S. Inouye, M. R. Andrews, H.-J. Miesner, D. M. Stamper-Kurn, and W. Ketterle, Strongly enhanced inelastic collisions in a Bose-Einstein condensate near Feshbach resonances, Phys. Rev. Lett. **82**, 2422 (1999).

[75] R. Chapurin, X. Xie, M. J. Van de Graaff, J. S. Popowski, J. P. D'Incao, P. S. Julienne, J. Ye, and E. A. Cornell, Precision test of the limits to universality in few-body physics, Phys. Rev. Lett. **123**, 233402 (2019).

[76] V. Vuletić, A. J. Kerman, C. Chin, and S. Chu, Observation of low-field Feshbach resonances in collisions of cesium atoms, Phys. Rev. Lett. **82**, 1406 (1999).

[77] C. Chin, V. Vuletic, A. J. Kerman, and S. Chu, High resolution Feshbach spectroscopy of cesium, Phys. Rev. Lett. **85**, 2717 (2000).

[78] P. J. Leo, C. J. Williams, and P. S. Julienne, Collision properties of ultracold cesium 133 atoms, Phys. Rev. Lett. **85**, 2721 (2000).

[79] C. Chin, A. J. Kerman, V. Vuletic, and S. Chu, Determination of atomic scattering lengths from measurements of molecular binding energies near Feshbach resonance, Phys. Rev. Lett. **90**, 033201 (2003).

[80] M. D. Lee, T. Kohler, and P. S. Julienne, Excited Thomas-Efimov levels in ultracold gases, Phys. Rev. A **76**, 012720 (2007).

[81] T. Weber, J. Herbig, M. Mark, H.-C. Nagerl, and R. Grimm, Bose-Einstein condensation of cesium, Science **299**, 232 (2003).

[82] A. D. Lange, K. Pilch, A. Prantner, F. Ferlaino, B. Engeser, H.-C. Nagerl, R. Grimm, and C. Chin, Determination of atomic scattering lengths from measurements of molecular binding energies near Feshbach resonance, Phys. Rev. A **79**, 013622 (2009).

[83] G. H. Rawitscher, Jr., B. Esry, E. Tiesinga, J. Burke, Jr., and I. Koltracht, Comparison of numerical methods for the calculation of cold atom collisions, J. Chem. Phys. **111**, 10418 (1999).

[84] R. A. Gonzales, J. Eisert, I. Koltracht, M. Neumann, and G. Rawitscher, Integral equation method for the continuous spectrum radial Schrödinger equation, J. Comput. Phys. **134**, 134 (1997).

[85] J. P. Burke, Jr., C. H. Greene, and B. D. Esry, Multichannel spectrum of neutral particles trapped by a wire, Phys. Rev. A **54**, 3225 (1996).

[86] K.-J. Bathe and E. L. Wilson, *Numerical Methods in Finite Element Analysis* (Prentice Hall, Englewood Cliffs, NJ, 1976).

[87] C. H. Greene, Atomic photoionization in a strong magnetic field, Phys. Rev. A **28**, 2209 (1983).

[88] R. G. Gordon, New method for constructing wavefunctions for bound states and scattering, J. Chem. Phys. **51**, 14 (1969).

[89] W. H. Press, S. A. Teukolsky, W. T. Vetterling, and B. P. Flannery, *Numerical Recipes in FORTRAN; The Art of Scientific Computing*, 2nd ed. (Cambridge University Press, Cambridge, 1993).

[90] Z. Zlatev, I. Dimov, I. Faragó, K. Georgiev, and Ágnes Havasi, Explicit Runge–Kutta methods combined with advanced versions of the Richardson extrapolation, Comput. Methods Appl. Math. **20**, 739 (2020).